Composites Part B 281 (2024) 111571

Contents lists available at ScienceDirect

Composites Part B

journal homepage: www.elsevier.com/locate/composites

Micromechanics stiffness upscaling of plant fiber-reinforced composites

Markus Königsberger [a,*], Valentin Senk [a], Markus Lukacevic [b,a], Michael Wimmer [c], Josef Füssl [a]

[a] Institute for Mechanics of Materials and Structures, TU Wien, Vienna, Austria
[b] Christian Doppler Laboratory for Next-Generation Wood-Based Biocomposite, TU Wien, Vienna, Austria
[c] Institute of Computer Graphics and Algorithms, TU Wien, Vienna, Austria

ARTICLE INFO

Keywords:
Biocomposite
Multiscale modeling
Natural fibers
Young's modulus
Elasticity
Weak interface
Fiber orientation

ABSTRACT

Fiber-reinforced green composites made from natural plant fibers are an increasingly popular sustainable alternative to conventional high-performance composite materials. Given the variety of natural fibers themselves, and the even larger variety of possible composites with specific fiber dosage, fiber orientation distribution, fiber length distribution, and fiber–matrix bond characteristics, micromechanics-based modeling is essential for characterizing the macroscopic response of these composites. Herein, an analytical multiscale micromechanics model for elastic homogenization is developed, capable of capturing the variety. The model features (i) a nanoscopic representation of the natural fibers to predict the fiber stiffness from the universal stiffness of the fiber constituents, mainly cellulose, (ii) a spring-interface model to quantify the compliance of the fiber–matrix bond, and (iii) the ability to model any (and any combination of) orientation distribution and aspect ratio distribution. Validation is performed by comparing the predicted stiffness to experimental results for as many as 73 composites available in the literature. Extensive sensitivity analyses quantify the composite stiffening upon increasing fiber volume fraction, fiber alignment, fiber length, and fiber–matrix interface stiffness, respectively.

1. Introduction

Biocomposites made from cellulose-based natural plant fibers have proven to be a sustainable and cost-effective alternative in several engineering fields [1–4]. These composites consist of abundantly available natural fibers that are glued together by a polymer matrix. The stiffness of plant fibers varies significantly, ranging from less than 10 GPa for coir or oil palm leaf fibers [5,6] to 100 GPa for bast fibers such as flax or ramie [2,7], and are thus comparable to synthetic E-glass fibers. The mechanical properties of plant fiber-reinforced composites, in turn, vary even more, as they further depend on the composite mix design, the matrix selection, and the composite manufacturing process [3,8].

Despite the variety, all plant fiber-reinforced composites share notably similar microstructural characteristics. Elongated fibers with different degrees of alignment are embedded in a matrix material at the composite scale. The morphometric parameters, such as fiber dosage, fiber length (and diameter), and its distribution, or the fiber orientation distribution vary, within broad ranges. Moreover, all plant fibers themselves share a common microstructural fingerprint [5,8]. Technical fibers used for composite manufacturing are typically actually fiber bundles and . One individual fiber is formed by a central lumen, surrounded by a lignocellulosic cell wall material including lignin, hemicellulose, and – most importantly – cellulose microfibrils that are characteristically misaligned with respect to the fiber direction. However, the morphometric parameters such as the angle between the parallel microfibrils and the fiber axis or the lumen porosity vary from plant to plant.

Given the microstructural similarities at both the composite and the fiber scale, micromechanics modeling is a suitable vehicle for linking microstructure to macro-properties. It allows the prediction of the influence of the morphometric parameters on the composite properties and is thus able to systematically explain the varying composite stiffness encountered in experimental testing campaigns. Considering the number of possible combinations of matrix and fiber materials, different composite production techniques, and different fiber treatments, micromechanics modeling techniques provide a very valuable addition to expensive experimental assessments.

The micromechanical modeling of plant fiber-reinforced biocomposites, despite the advances in composite mechanics [9], still relies primarily on empirical or semi-empirical approaches [10–13], such as (modified) mixture rules, the Hirsch model [14], the Cox–Krenchel model [15,16], or the Halpin–Tsai model [17]. In addition to the empirical nature of some underlying parameters, these approaches typically assume a perfect bond between fiber and matrix. They are further typically limited to specific fiber orientation distributions (such as parallel fibers) and often cannot accommodate fibers of different lengths.

* Corresponding author.
E-mail address: markus.koenigsberger@tuwien.ac.at (M. Königsberger).

https://doi.org/10.1016/j.compositesb.2024.111571
Received 30 December 2023; Received in revised form 6 May 2024; Accepted 15 May 2024
Available online 20 May 2024
1359-8368/© 2024 The Authors. Published by Elsevier Ltd. This is an open access article under the CC BY license (http://creativecommons.org/licenses/by/4.0/).

Herein, we aim to overcome these limitations by applying advanced continuum micromechanics-based homogenization techniques [18] to predict the 3D stiffness tensor of biocomposites. We target a model that can quantify the gain or reduction of the biocomposite stiffness upon changing physico-chemical fiber properties. This includes selecting different fiber species or different fiber processing or treatment methods. Additionally, the model should allow the change of the matrix, the fiber volume fraction, the fiber orientation distributions, or the fiber–matrix bond properties. Therefore, we build upon a recently developed multiscale micromechanics approach [19] for predicting the stiffness of plant fibers from the intrinsic micro-structure with plant-specific morphometric parameters and chemical composition. Notably, the stiffness of all constituents [cellulose (in crystalline or amorphous form), lignin, hemicelluloses, pectin, pores, and inorganics [1]] is considered intrinsic and determined by atomistic simulations or small-scale experiments.

In this paper, we extend this approach to the composite scale. We represent fibers by spheroidal inclusions and consider them to be embedded in a polymer matrix. The interface between matrix and fiber is potentially weakened, a typical feature of plant fiber-reinforced composites [20,21]. Fibers are considered to exhibit any orientation distribution, i.e., they may be fully aligned (all fibers are parallel), oriented randomly in all space directions, or they may exhibit any orientation distribution in between these two limit cases, to account for the various possible degrees of alignment observed experimentally [22]. Moreover, fiber aspect ratios (length-to-diameter ratios) may also be distributed, most typically with asymmetric distribution functions [23].

2. Multiscale micromechanics modeling of biocomposites

2.1. Micromechanics representation

Relying on classical homogenization theory [18], biocomposites are considered as a statistically homogeneous body at a macroscopic observation scale but as an heterogeneous material that can be described by a representative volume element (RVE) at the microscopic observation scale. RVE and macroscopic material point behave identically under any mechanical loads. This can be ensured only if the characteristic size of any RVE is, on the one hand, considerably larger than the characteristic size of any of the inhomogeneities (defined as material phases with intrinsic and known physical quantities) inside the RVE and, on the other hand, considerably smaller than the entire biocomposite structure. To portray the microstructural heterogeneity of biocomposites, a multiscale representation is adopted, that extends this scale-separation principle to RVEs at multiple length scales.

We model biocomposites by means of five RVEs distributed across four scales of observation, see Fig. 1. At the largest scale, the RVE "biocomposite" with a characteristic length of several centimeters is considered to contain three phases: technical (natural) fibers, macroscopic pores, which are unavoidable during composite production [24,25], and a (biodegradable) matrix material surrounding fibers and pores. Most notably, the weak bond between fiber and matrix, often encountered in composites with natural fibers [20,21], is incorporated into the model by considering imperfect bonding by means of a linear spring interface model with vanishing thickness [26]. Thus, displacement jumps $[\underline{u}]$ are allowed and considered proportional to continuous tractions as [27]

$$[\underline{u}] = \boldsymbol{\eta} \cdot \boldsymbol{\sigma} \cdot \underline{n} \tag{1}$$

with $\boldsymbol{\sigma}$ as stress tensor, $\underline{n}$ as unit normal vector, and $\boldsymbol{\eta}$ as second-order interface compliance tensor with components reading as [26]

$$\eta_{ij} = \alpha\delta_{ij} + (\beta - \alpha)\, n_i n_j \,. \tag{2}$$

In Eq. (2), $\alpha \geq 0$ and $\beta \geq 0$ denote the compliance coefficient related to tangential sliding and normal separation, respectively, and δ_{ij} is the Kronecker delta. Notably, $\alpha > 0$ and $\beta = 0$ characterizes tangential displacement jumps only, while $\alpha = 0$ and $\beta > 0$ characterizes normal displacement jumps. It may be more convenient to normalize the interface compliance by the fiber radius (or by half of the fiber diameter d_f), i.e., we define normalized interface compliances $\overline{\alpha} = 2\alpha/d_f$ and $\overline{\beta} = 2\beta/d_f$.

The fibers are considered as prolate spheroids defined by an aspect ratio a as the quotient of fiber length l_f and fiber diameter d_f, $a = l_f/d_f \geq 1$. The fiber aspect ratios in a biocomposite are not constant. Rather, they vary from one fiber to another [22]. To capture the variety, several different aspect ratio distributions are considered herein, among which the lognormal distribution fits well to microscopy results of several different natural fiber-reinforced composites [21,23] (see Appendix A for mathematical details).

The fiber orientation, one of the critical parameters for the homogenized stiffness [28], is mathematically considered by means of fiber orientation distribution functions $f_o(\varphi, \vartheta)$, which are non-negative functions defined on the unit sphere with respect to azimuth angle φ and zenith angle ϑ, defined in the global Cartesian coordinate system x, y, z, see Fig. 1. Typical orientation distribution functions for (short) fiber-reinforced composites are the transversally isotropic "von Mises-Fisher" distribution (see Appendix B for mathematical details and visualizations), which is able to capture the preferred orientation of fibers along a single axis, as often found in microscopic images of extruded [22], pultruded [29], or 3D printed [30] biocomposites. For biocomposites produced by the film-stacking method, thin fiber mats with in-plane random orientation distribution are stacked and filled with the polymeric matrix material. This results in another rotationally symmetric orientation distribution, but with a preferred orientation along a plane, for which the "von Mises" distribution is adopted. As for injection-moulded biocomposites with complex shapes, the typically inhomogeneous orientation distribution depends on the production speed and the geometry of the part. In any case, the actual fiber orientation can either be measured, for instance by granulometry [31], or modeled by means of computation fluid dynamics [32].

The microstructure of the technical fibers itself is resolved at smaller observation scales, see Fig. 1, following the recently developed multiscale model of Königsberger et al. [19]. Thereby, we exploit the fact that despite the widely different mechanical properties of natural fibers [2], they all share a common microstructural fingerprint [5]. The fiber microstructure is built up by a handful of virtually intrinsic constituents, mostly cellulose, hemicellulose, lignin, and pores. The fiber stiffness is predicted from the fiber-specific volume dosage of these constituents as well as from the fiber-specific geometric features, following a recently developed multiscale micromechanical model for plant fibers [19], which originates from earlier works on wood [33,34] and plant culms [35], and is shortly summarized next. At the scale of several tens of microns, we consider the technical fibers as fiber bundles, which consist of a cell wall matrix with embedded cylindrical lumen porosity aligned with the longitudinal fiber direction L. At the scale of a single micron, the cell wall is resolved to consist of cylindrical cellulose microfibrils embedded in a matrix of polymer network. The cellulose microfibrils and the plant fibers (with coordinate base R, T, L) are typically not aligned. Rather, the microfibrils are considered to be inclined by a (constant) microfibril angle $\overline{\theta}$, defined as the angle between the microfibril orientation l and the longitudinal plant fiber direction L, see the orientations indicated below the RVEs in Fig. 1. The microfibril orientation with respect to the R-T-plane is uniformly distributed. At the nanoscale, two RVEs are considered. The cellulose is considered as a matrix-inclusion composite with stiff aligned crystalline nanofibrils, modeled as cylinders, which are embedded in a much softer amorphous matrix. The polymer network, in turn, consists of five spherical phases: hemicellulose, lignin, pectin, nanopores (initially filled with extractives (including waxes, oils, and fats), and potentially emptied during fiber processing), and ashes (inorganic parts). In contrast to the interface around the technical fibers, all interfaces at the smaller scales are characterized by perfect bonding. Notably, the stiffness of all phases, including the technical fibers, is transversally isotropic [19].

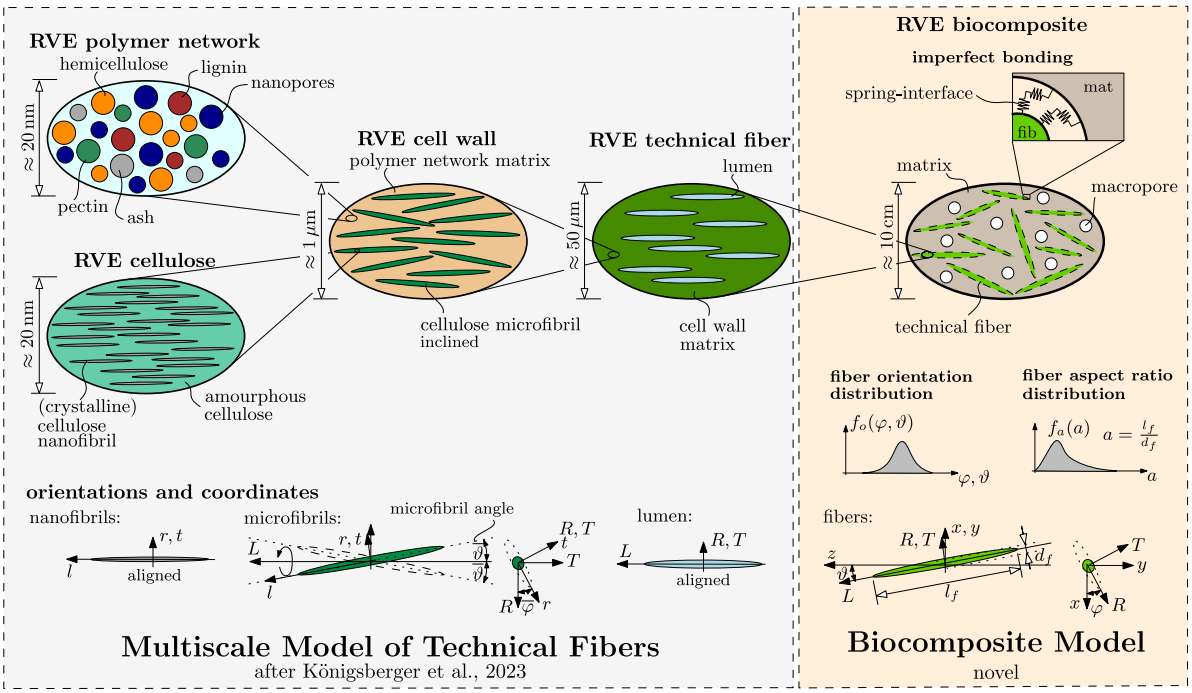

Fig. 1. Multiscale representation of biocomposites.

2.2. Stiffness homogenization

2.2.1. Matrix-inclusion problem with imperfect interfaces

A continuum micromechanics approach [18] is adopted to homogenize the linear elastic stiffness of the RVEs introduced before. They are characterized by spheroidal microscopic phases with transversally isotropic stiffness, potentially spring-type interface behavior according to (1) and (2), and may exhibit any orientation distribution, and any aspect ratio distribution. The first step in continuum micromechanics towards finding a stiffness homogenization rule for the RVE is the consideration of Eshelby-type matrix-inclusion problems [36], where a single elastic inclusion (stiffness tensor $\mathbb{C}_i$) is embedded in an elastic infinite matrix (stiffness tensor $\mathbb{C}_0$). In our case with continuous orientation and aspect ratio distributions, infinitely many Eshelby-type matrix-inclusion problems with imperfect (spring-type) interfaces [26,37] are introduced, such that one Eshelby problem exists for each spheroidal sub-phase, i.e., for each phase of the RVE with specific aspect ratio a and specific orientation (in terms of position angles φ, ϑ). In each Eshelby problem, the inclusion's stiffness, aspect ratio, and orientation are equal to the respective property of the material sub-phase in the RVE. By analogy, the spring-type interface properties in the Eshelby problem with continuous tractions and displacement jumps according to (1) are equal to the properties of the interface between the inclusion phase and surrounding matrix phase in the corresponding RVE. We are left with specifying the stiffness of the infinite matrix $\mathbb{C}_0$ in the matrix-inclusion problems. The matrix stiffness is typically either set equal to the stiffness of a matrix phase which might be present in the RVE and which hosts all other heterogeneities ("Mori–Tanaka-type" homogenization scheme for matrix-inclusion-type materials [18,38,39]); or $\mathbb{C}_0$ is equal to the homogenized stiffness of the RVE, $\mathbb{C}_{\text{hom}}$ if all phases interact mutually (self-consistent homogenization scheme for polycrystalline materials [40,41]).

We are first interested in relating homogeneous strains $\boldsymbol{E}_0$ at the outer boundary to average strains of the inclusion ($\widetilde{\boldsymbol{\varepsilon}}_i$) and average strains in the interface ($\widetilde{\boldsymbol{\varepsilon}}_{i/0}$), the latter being defined as [42]

$$\widetilde{\varepsilon}_{i/0,kl} = -\frac{1}{2V_i}\int_{S_i}\left(\left[u_k\right]n_l + \left[u_l\right]n_k\right)\,dS\,, \tag{3}$$

with V_i and S_i as volume and surface of the spheroid, $\boldsymbol{\eta}$ as interface compliance according to (2), and $\underline{n}$ as unit normal vector pointing outward (from the spheroid to the surrounding matrix). In case of vanishing displacement jumps across the interface (perfect bond), the interface strains vanish and the inclusion strains $\widetilde{\boldsymbol{\varepsilon}}_i$ are uniform [36]. This uniformity is lost for imperfectly bonded interfaces. However, it is typically assumed to be constant to obtain a solution for the spring-type interface behavior [26,37,43]. This limits the approach to slightly weakened interfaces with small interface compliance $\boldsymbol{\eta}$ [26]. Adopting this assumption, the average interface strains $\widetilde{\boldsymbol{\varepsilon}}_{i/0}$ can be linked to the uniform inclusion strains $\widetilde{\boldsymbol{\varepsilon}}_i$ according to [44]

$$\widetilde{\boldsymbol{\varepsilon}}^{i/0}(\varphi,\vartheta;a) = -\mathbb{R}^{i/0} : \mathbb{C}_i : \widetilde{\boldsymbol{\varepsilon}}_i(\varphi,\vartheta;a) \tag{4}$$

where $\mathbb{R}^{i/0}$ is a fourth-order tensor which components, for spring-type interfaces, read as [26,37]

$$R_{i/0,ijkl} = \frac{1}{4V_i}\int_{S_i}\eta_{ij}n_kn_l + \eta_{ik}n_jn_l + \eta_{jk}n_in_l + \eta_{il}n_jn_k\,dS \tag{5}$$

As for the computation of the components of $R_{i/0}$, we refer to Refs. [26,45]. The approximately uniform strains of the spheroidal inclusions, oriented in (φ,ϑ)-direction and exhibiting aspect ratio a, then reads as [44]

$$\widetilde{\boldsymbol{\varepsilon}}_i(\varphi,\vartheta;a) = \mathbb{A}_{i,0}(\varphi,\vartheta;a) : \boldsymbol{E}_0\,. \tag{6}$$

with $\mathbb{A}_{i,0}$ as strain concentration tensor reading as [44]

$$\mathbb{A}_{i,0}(\vartheta,\varphi;a) = \Big\{\mathbb{I} + \mathbb{S}_i(\vartheta,\varphi;a) : \left(\mathbb{C}_0\right)^{-1}\left[\mathbb{C}_i(\vartheta,\varphi) - \mathbb{C}_0\right] + \left[\mathbb{I} - \mathbb{S}_i(\vartheta,\varphi;a)\right] : \mathbb{R}_{i/0}(a) : \mathbb{C}_i(\vartheta,\varphi)\Big\}^{-1}\,. \tag{7}$$

In Eq. (7), $\mathbb{I}$ is the fourth-order unity tensor, $\mathbb{S}_i$ is the fourth-order Eshelby tensor (identical to the case of perfect interfaces). Notably, if the interface compliance vanishes (perfect bond), tensor $\mathbb{R}_{i/0}$ vanishes, and the strain concentration tensor $\mathbb{A}_{i,0}$ reduces to its classical form. Analytical formulas for the components of $\mathbb{S}_i$ and $\mathbb{R}_{i/0}$ for spheroidal phases are given in Appendix C.

2.2.2. RVEs with phases containing imperfect interfaces

Next, we move back from the matrix-inclusion problem to the actual RVEs containing multiple linear elastic, transversally isotropic,

spheroidal phases with phase volume fractions $f_i = V_i/V_{\text{tot}}$, satisfying $\sum_{i=1}^{N} f_i = 1$, where each phase exhibits aspect ratio distribution f_a and orientation distribution f_o. All phases obey Hooke's law

$$\boldsymbol{\sigma}_i = \mathbb{C}_i : \boldsymbol{\varepsilon}_i \,, \tag{8}$$

with $\boldsymbol{\sigma}_i$ and $\boldsymbol{\varepsilon}_i$ as (volume) averages of phase stresses and strains, and $\mathbb{C}_i$ as transversally isotropic phase stiffness tensor. Average rules of equilibrated stresses and compatible strains inside the RVE containing N imperfectly bonded phases imply [18]

$$\sum_{i=1}^{N} f_i \, \boldsymbol{\sigma}_i = \boldsymbol{\Sigma} \tag{9}$$

and [44]

$$\sum_{i=1}^{N} f_i \, \left(\boldsymbol{\varepsilon}_i - \boldsymbol{\varepsilon}_{i/0}\right) = \boldsymbol{E} \tag{10}$$

where the $\boldsymbol{\varepsilon}_{i/0}$ denotes the average interphase strains resulting from the displacement jumps according to Eq. (3). In continuum micromechanics, the average strains $\boldsymbol{\varepsilon}_i$ (and stresses) in any phase i of the RVE are considered to be equal to the strains $\widetilde{\boldsymbol{\varepsilon}}_i$ (and stresses) of the infinite matrix-inclusion problem containing an inclusion mimicking phase i, according to Eq. (6). By analogy, the interface strains $\boldsymbol{\varepsilon}_{i/0}$ in the RVE are considered equal to the interface strains $\widetilde{\boldsymbol{\varepsilon}}_{i/0}$ in the corresponding matrix-inclusion problem according to Eq. (4). Thus, the strain average rule (10) is rewritten considering Eqs. (4) and (6), yielding a link between the unknown boundary strains in the matrix inclusion problem $\boldsymbol{E_0}$ and the RVE strains $\boldsymbol{E}$ as

$$\boldsymbol{E}_0 = \left[\sum_{i=1}^{N} f_i \left(\mathbb{I} + \mathbb{R}_{i/0}(a) : \mathbb{C}_i\right) : \mathbb{A}_{i,0}(\varphi, \vartheta; a)\right]^{-1} : \boldsymbol{E} \,. \tag{11}$$

Finally, the stress average rule (9) is combined with the microscopic Hooke's law (8) and strain concentration relation (6) and the link derived in Eq. (11). After comparison with the macroscopic Hooke's law $\boldsymbol{\Sigma} = \mathbb{C}_{\text{hom}} : \boldsymbol{E}$, an expression for the sought homogenized stiffness $\mathbb{C}_{\text{hom}}$ for RVE containing N spheroidal phases exhibiting aspect ratio density $f_a(a)$, orientation distribution $f_o(\vartheta, \varphi)$, and transversally isotropic stiffness tensor $\mathbb{C}_i$ is obtained, reading as [46]

$$\mathbb{C}_{\text{hom}} = \sum_{i=1}^{N} f_i \int_0^{\infty} f_a(a) \int_0^{2\pi} \int_0^{\pi} f_o(\vartheta, \varphi) \, \mathbb{C}_i(\vartheta, \varphi) : \mathbb{A}_i(\vartheta, \varphi; a) \sin\vartheta \, \mathrm{d}\vartheta \, \mathrm{d}\varphi \, \mathrm{d}a \tag{12}$$

In Eq. (12), $\mathbb{A}_i$ is the RVE phase strain concentration tensor and reads as

$$\mathbb{A}_i(\vartheta, \varphi; a) = \mathbb{A}_{0,i}(\vartheta, \varphi; a) : \left[\sum_{i=1}^{N} f_i \int_0^{\infty} f_a(a) \int_0^{2\pi} \int_0^{\pi} f_o(\vartheta, \varphi) \times \left(\mathbb{I} + \mathbb{R}_{i/0}(a) : \mathbb{C}_i\right) : \mathbb{A}_{0,i}(\vartheta, \varphi; a) \sin\vartheta \, \mathrm{d}\vartheta \, \mathrm{d}\varphi \, \mathrm{d}a\right]^{-1} , \tag{13}$$

2.2.3. Application to biocomposites

Bottom-up stiffness homogenization according to Eq. (12) with strain concentration tensors (13) and (7) is now applied to the RVEs depicted in Fig. 1. The homogenized stiffness of the polymer network $\mathbb{C}_{pn}$ follows from specialization of homogenization rule (12) for five spherical and isotropic phases hemicellulose, lignin, pectin, wax, and ash, with perfectly bonded interfaces (resulting in $\mathbb{R}_{i/0} = 0$), and for the self-consistent homogenization scheme ($\mathbb{C}_0 = \boldsymbol{C}_{pn}$). The resulting equation of the homogenized stiffness of this RVE and all others are given in Appendix C in full detail. The cellulose microfibril stiffness $\mathbb{C}_{celMF}$ results from considering the Mori–Tanaka scheme with cylindrical and aligned crystalline cellulose phases perfectly bonded to the amorphous cellulose matrix. These two nanoscale homogenization results allow for predicting the homogenized stiffness of the cell wall $\mathbb{C}_{cw}$, considering that cylindrical cellulose microfibrils are perfectly bonded to a polymer network matrix in a Mori–Tanaka setting. The homogenized stiffness of the fiber $\mathbb{C}_{fib}$ follows from the specialization of homogenization rule using a Mori–Tanaka scheme with cylindrical and aligned lumen pores embedded in a cell wall matrix (homogenized before). Finally, the sought homogenized stiffness of the biocomposite $\mathbb{C}_{comp}$ follows from adopting yet another Mori–Tanaka scheme considering that the polymer matrix phase hosts spherical pores and spheroidal fibers. Notably, any fiber orientation distribution function f_o, any fiber aspect ratio distribution f_a, and imperfect interfaces according to Eqs. (1) and (2) are considered.

2.3. Intrinsic phase stiffnesses

We aim for stiffness upscaling from the nanoscale, where phase properties (stiffness, density) are considered intrinsic, i.e., constants, which do not change from one fiber to another. The stiffness of crystalline Iβ cellulose is obtained from molecular dynamics simulations [47], which are approximated to be transversally isotropic [33], with stiffness tensor components referring to the local microfibril base system $\underline{r}, \underline{t}, \underline{l}$ amounting to

$$\mathbb{C}_{\text{crycel}} = \begin{bmatrix} C_{rrrr} = 34.86 & 0 & 0 & 0 & 0 & 0 \\ 0 & 34.86 & 0 & 0 & 0 & 0 \\ 0 & 0 & 167.8 & 0 & 0 & 0 \\ 0 & 0 & 0 & 2\,C_{tltl} = 11.61 & 0 & 0 \\ 0 & 0 & 0 & 0 & 11.61 & 0 \\ 0 & 0 & 0 & 0 & 0 & 34.86 \end{bmatrix}_{\underline{e}_r, \underline{e}_t, \underline{e}_l} \times \text{GPa} \,. \tag{14}$$

All other intrinsic phases are considered to be isotropic, with phase stiffness tensors $\mathbb{C}_i$ reading as

$$\mathbb{C}_i = 3\,k_i \mathbb{I}_{\text{vol}} + 2\,\mu_i \mathbb{I}_{\text{dev}} \tag{15}$$

where k_i and μ_i are the bulk and the shear moduli of phase i, obtained from experiments such as nanoindentation tests [48,49] or molecular models [50], as summarized in Table 1. Since many different materials are used as polymer matrices at the composite scale, its stiffness is adapted accordingly; see Section 3 for details. Typical Young's moduli E_{pm} and Poisson's ratios ν_{pm} (which readily translate to bulk and shear moduli used to construct the stiffness tensor $\mathbb{C}_{\pm}$) of common polymers are summarized in Table 1 and are used for modeling if the experiments do not provide further information.

2.4. Composite-specific input properties: volume fractions and geometric properties

Plant-specific chemo-physical fiber properties were collected from chemical analysis (including acid hydrolysis, chromatography, Klason lignin analysis, and thermogravimetric analysis) by Königsberger et al. [19] for 27 of the most common plant fibers, grouped into five fiber types: bast (banana, fiber flax, hemp, isora, jute, kenaf, ramie, sorghum), grass (alfa, bagasse, bamboo), leaf (abaca, curaua, henequen, phormium/harekeke, pineapple, sisal), fruit or seeds (coir, cotton, kapok, oil palm), and straw (barley, cornhusk, cornstalk, rice, soybean, wheat). Given the variety of the fiber properties due to varying species, location, climate, processing etc., fiber and composite stiffnesses are predicted for three representative cases: properties which refer to a minimum stiffness, an average stiffness, and a maximum stiffness, where the cases refer to a biocomposite with parallel fibers. Cell wall volume fractions corresponding to the minimum case are obtained from minimum reported cellulose mass fractions and minimum reported crystallinities. By analogy, maximum cellulose mass fractions and maximum reported crystallinities are used to obtain cell wall volume fractions for the maximum case. Average fractions, in turn, are obtained from the averages of the reported properties. This

Table 1
Densities ρ_i as well as elastic properties (bulk moduli k_i and shear moduli μ_i of all constituents of natural fibers and pores; Young's moduli E_{pm} and Poisson's ratios ν_{pm} of the different polymers used frequently); properties refer to dry or nearly dry matter; values of nanoscopic phases are also used in Königsberger et al. [19].

constituent phase	i	ρ_i [g/cm^3]	Ref.	k_i [GPa]	μ_i [GPa]	Ref.
crystalline cellulose	crycel	1.59	[51]	Anisotropic, see Eq. (14)		[47]
amorphous cellulose[c]	amcel	1.50	[52]	6.22	2.07	[50]
hemicellulose[c]	hemcel	1.46	[53]	8.08	3.73	[53,54]
lignin	lig	1.27	[53]	5.00	2.31	[53,55]
pectin[b]	pec	1.53	[56]	1	0.4	
ash[a]	ash	2.20	[57]	36.3	30.9	[57]
nanopores (extractives)	npor	0.9	[33]	0	0	
lumen pores (air-filled)	lpor	0		0	0	
macropores (air-filled)	mpor	0		0	0	
polymer matrix phase[d]	pm	ρ_i [g/cm^3]	Ref.	E_i [GPa]	ν_i [–]	Ref.
PP (MAPP)		0.89	[58]	1.89	0.43	[22,59]
PLA				3.50	0.33	[60,61]
HDPE				1.20	0.46	[59,62]
Epoxy		1.16	[63]	3.91	0.32	[63,64]
Polyamid [65]				1.14	0.4[e]	

[a] Properties of amorphous silica (silica glass) are considered representative.
[b] Elastic properties assumed.
[c] Poisson's ratio assumed to be 0.35 [33]
[d] The actual properties may depend on the exact type of polymer and are adapted in the validation section if the experiments include additional information.
[e] Poisson's ratios of Polyamid and other polymers are assumed to be 0.4, if no values are found in the literature.

Table 2
Calculated cell wall-related phase volume fractions f_i^{cw} in percent related to the cases minimum/**average**/maximum homogenized stiffness.

Name	Type	cry. cell.	am. cell.	hemicell.	lignin	pectin	ash	nanopore
Banana	B	18/**31**/40	41/**38**/40	14/**10**/6	13/**10**/6	5/**4**/2	5/**3**/2	5/**3**/2
Flax	B	32/**54**/70	32/**15**/8	21/**18**/13	4/**4**/3	1/**1**/1	0/**0**/0	10/**8**/6
Hemp	B	27/**50**/76	27/**17**/2	28/**20**/13	8/**6**/4	1/**1**/1	0/**0**/0	9/**7**/4
Isora	B	21/**46**/54	40/**19**/17	3/**3**/2	27/**24**/20	0/**0**/0	0/**0**/0	9/**8**/7
Jute	B	26/**37**/51	14/**16**/16	22/**18**/12	26/**20**/14	0/**0**/0	0/**0**/0	12/**9**/7
Kenaf	B	17/**34**/55	11/**18**/23	33/**22**/10	29/**19**/9	3/**2**/1	0/**0**/0	7/**5**/2
Ramie	B	39/**49**/62	27/**28**/28	22/**14**/7	2/**1**/1	3/**2**/1	0/**0**/0	8/**5**/2
Sorghum	B	19/**27**/36	40/**36**/32	22/**20**/17	13/**12**/10	0/**0**/0	4/**3**/3	2/**2**/1
Alfa	G	17/**21**/26	11/**12**/11	32/**30**/28	37/**35**/32	0/**0**/0	0/**0**/0	3/**3**/2
Bagasse	G	12/**15**/23	16/**17**/20	23/**21**/18	8/**7**/6	9/**9**/7	3/**2**/2	30/**28**/24
Bamboo	G	10/**16**/24	15/**13**/16	20/**19**/16	28/**26**/22	0/**0**/0	0/**0**/0	27/**26**/22
Abaca	L	24/**30**/38	27/**28**/28	23/**20**/16	12/**10**/8	1/**1**/1	2/**1**/1	11/**10**/8
Curaua	L	38/**45**/53	24/**23**/21	12/**10**/8	11/**9**/7	0/**0**/0	0/**0**/0	15/**13**/11
Henequen	L	23/**28**/34	32/**32**/31	26/**23**/20	10/**9**/8	0/**0**/0	1/**1**/1	9/**8**/7
Phormium	L	34/**41**/47	20/**19**/17	32/**29**/25	14/**12**/11	0/**0**/0	0/**0**/0	0/**0**/0
Pineapple	L	28/**36**/50	36/**33**/34	20/**18**/9	10/**9**/5	4/**4**/2	1/**1**/0	0/**0**/0
Sisal	L	23/**42**/67	11/**16**/19	22/**14**/5	21/**14**/4	15/**9**/3	0/**0**/0	8/**5**/2
Coir	F	5/**11**/15	15/**25**/29	23/**18**/16	46/**37**/32	4/**3**/3	7/**6**/5	0/**0**/0
Kapok	F	18/**23**/31	26/**27**/30	29/**27**/21	19/**17**/14	0/**0**/0	1/**1**/0	6/**6**/4
Oil Palm	F	8/**11**/18	32/**34**/43	25/**22**/16	22/**19**/14	0/**0**/0	3/**2**/2	11/**10**/7
Barley	S	12/**17**/22	15/**17**/18	34/**31**/28	20/**18**/16	0/**0**/0	0/**0**/0	20/**18**/16
Cornhusk	S	22/**39**/59	24/**14**/0	38/**33**/29	4/**4**/3	0/**0**/0	6/**6**/5	6/**5**/4
Cornstalk	S	15/**25**/37	14/**8**/0	27/**25**/24	15/**15**/14	0/**0**/0	0/**0**/0	29/**28**/26
Rice	S	10/**18**/22	15/**12**/12	27/**26**/24	16/**15**/14	0/**0**/0	12/**11**/10	20/**19**/18
Soybean	S	14/**38**/45	19/**43**/42	18/**5**/3	45/**13**/9	0/**0**/0	5/**1**/1	0/**0**/0
Wheat	S	12/**16**/20	14/**15**/15	28/**26**/24	20/**19**/17	0/**0**/0	0/**0**/0	26/**25**/23

way, a minimum, an average (bold values), and a maximum of the cell wall-related phase volume fraction is obtained for all 27 fibers, see Table 2 for the results and Königsberger et al. [19] for details about the derivation.

RVE-specific volume fractions, occurring in homogenization Eqs. (C.5)–(14), are derived next. Cell wall-related volume fractions of polymer network (f_{pn}^{cw}) and of the cellulose microfibrils (f_{celMF}^{cw}) read as [19]

$$f_{pn}^{cw} = f_{hemcel}^{cw} + f_{lig}^{cw} + f_{pec}^{cw} + f_{ash}^{cw} + f_{npor}^{cw}, \quad f_{celMF}^{cw} = f_{crycel}^{cw} + f_{amcel}^{cw}. \tag{16}$$

Polymer network-related volume fractions of hemicellulose (f_{hemcel}^{pn}), lignin (f_{lig}^{pn}), pectin (f_{pec}^{pn}), ash (f_{ash}^{pn}), and nanoporosity (f_{npor}^{pn}) read as [19]

$$f_i^{pn} = \frac{f_i^{cw}}{f_{pn}^{cw}}, \quad i \in \{hemcel, lig, pec, ash, npor\}, \tag{17}$$

and cellulose-related volume fractions of crystalline (f_{crycel}^{cel}) and amorphous (f_{amcel}^{cel}) cellulose read as [19]

$$f_i^{cel} = \frac{f_i^{cw}}{f_{celMF}^{cw}}, \quad i \in \{crycel, amcel\}. \tag{18}$$

The fiber-related cell wall volume fraction f_{cw}^{fib} and the lumen volume fraction f_{lpor}^{fib} are obtained from the literature-reported fiber density as [19]

$$f_{cw}^{fib} = \frac{\rho_{fib}}{\rho_{cw}} \leq 1, \quad f_{lpor}^{fib} = 1 - \frac{\rho_{fib}}{\rho_{cw}} \geq 0, \tag{19}$$

with composition-dependent cell wall density reading as

$$\rho_{cw} = \sum_i \rho_i f_i^{cw}, \quad i \in \{crycel, amcel, hemcel, lig, pec, ash, npor\}. \tag{20}$$

Note that Eq. (20) is specialized for average phase volume fractions only, such that the resulting cell wall density is an average quantity.

Minimum, average, and maximum fiber-related volume fractions, respectively, then follow from evaluating Eq. (19) with average cell wall densities ρ_{cw}, but with reported minimum, average, and maximum fiber densities, respectively, see Königsberger et al. [19] for corresponding fiber densities and lumen porosities for all 27 plants.

Volume fractions related to the composite scale f_i^{comp} are discussed next. Composite mix design is typically reported in mass terms, with fiber mass fraction m_{fib}^{comp}, and polymer matrix mass fraction $m_{pm}^{comp} = 1-m_{fib}^{comp}$. If macroscopic air pores are disregarded, mass fractions can be translated into the volume fractions of fibers ($\tilde{f}_{fib}^{comp}$) and of the polymer matrix ($\tilde{f}_{fib}^{comp}$) according to

$$\tilde{f}_{fib}^{comp} = \frac{\rho_{pm}}{\frac{\rho_{fib}}{m_{fib}^{comp}-1} + \rho_{pm}}, \qquad \tilde{f}_{pm}^{comp} = 1 - \tilde{f}_{fib}^{comp}. \tag{21}$$

If air bubbles with volume fractions f_{mpor}^{comp} are entrapped during mixing, adjusted volume fractions of fibers (f_{fib}^{comp}) and of the polymer matrix (f_{fib}^{comp}) can be derived from the relations

$$f_{fib}^{comp} + f_{pm}^{comp} + f_{mpor}^{comp} = 1, \qquad \frac{f_{fib}^{comp}}{f_{pm}^{comp}} = \frac{\tilde{f}_{fib}^{comp}}{\tilde{f}_{pm}^{comp}} \tag{22}$$

yielding

$$f_{fib}^{comp} = \frac{1 - f_{mpor}^{comp}}{1 + \frac{\tilde{f}_{pm}^{comp}}{\tilde{f}_{fib}^{comp}}}, \qquad f_{pm}^{comp} = 1 - f_{fib}^{comp} - f_{mpor}^{comp}. \tag{23}$$

Finally, we report on the geometric input properties of the 27 plants introduced in the RVEs of Fig. 1, i.e., on microfibril angle, fiber length, fiber diameter, and fiber aspect ratio. Microfibril angles range from zero to 49°, see Table 3. If minimum and maximum values are not reported in the database, we assume a range of ±3° from the reported value. Plant-specific fiber dimensions are given in terms of a fiber length l_f and a fiber diameter d_f, see Table 3 for reported minimum, average, and maximum values. If only averages are reported, we assume a range of ±10%. Minimum, average, and maximum aspect ratios $a = l_f/d_f$ are obtained from suitable combinations. In more detail, the minimum aspect ratio follows from the minimum fiber length and the maximum fiber diameter, the average aspect ratio follows from the average dimension, and the maximum aspect ratio follows from the maximum fiber length and minimum diameter.

3. Model validation

3.1. Validation at the fiber scale

First, we revisit the validation at the fiber scale from Königsberger et al. [19] to highlight the good agreement between predicted and measured fiber modulus, a prerequisite for validation at the composite scale. The model-predicted elastic modulus (mean value, and interval between minimum and maximum) in axial fiber direction for all 26 studied natural fibers (see also Appendix E for all five independent fiber stiffness constants) is compared to experimental results from single-fiber tensile tests as documented in the literature (see Fig. 2).

Most predicted fiber moduli intervals agree very well with the experimentally measured counterparts. The model overestimates the experimental results for some fibers, particularly the leaf fibers. Note that the model assumes an imperfection-free technical fiber along all its length, an assumption which may be questionable for the very heterogeneous leaf fibers. Moreover, this overestimation may highlight the difficulties related to single-fiber testing, which results, e.g., from slippage [88], from misalignment [88], or from the imprecise measurement of the cross-sectional area of the fibers [85]. Lastly, some differences may also arise from neglected biochemical quantities when setting up the multiscale model, such as sugar contents, which are known to be partly responsible for the slightly smaller moduli for hemp compared to flax [90,91].

3.2. Validation at the composite scale

3.2.1. Strategy

After model validation attempts at the fiber scale, the predicted stiffness of the fiber-reinforced composite is next compared to the experimentally measured elastic moduli. Related experimental results are gathered from uniaxial tensile tests reported for many composites produced from different fibers and polymers by different production methods. Unsurprisingly, no experimental dataset exists that provides information on all necessary model input parameters; mechanical characterizations of the fiber–matrix interfaces are almost entirely lacking. Rather than comparing a single experiment to a somewhat calibrated model prediction, we aim at comparing sets of similar experiments from different research groups tested in various laboratories to modeling results with constant input properties. In more detail, the model is evaluated by assuming a perfect bond between fiber and matrix first. While several biocomposites show severe debonding along the fiber–matrix interfaces, only those data are included in the following subsection where no major bonding issues are reported. Only thereafter, comparisons regarding imperfect bonds are performed.

3.2.2. Perfect bond

First, interfaces are considered to be perfectly bonded. Spring-interface parameters α and β are thus considered to vanish, yielding a vanishing interface compliance according to Eq. (2), vanishing displacement jumps across the interface according to Eq. (1), and a vanishing interface tensor $\mathbb{R}^{fib-pm}$ appearing in homogenization Eq. (C.5). Corresponding experimental results are obtained from published literature data. Thereby, we carefully select experiments in which either no or only minor interface debonding has been reported, which is often achieved by functionalizing the polymer using a compatibilizer, for instance, maleic anhydride grafted polypropylene [23,105]. In total, data on 73 different composites were collected, produced from ten different plant species. While full details regarding the available input properties are presented in Table D.4 and the footnotes therein, we shortly highlight some key inputs next.

The dataset includes mainly flax fibers but also wheat, jute, henequen, phormium, sisal, alfa, and kenaf. Geometric fiber properties (fiber length and diameter) were typically reported by giving the average. Only Bourmaud et al. [22] provide full details on the actual distribution, allowing us to fit the measured aspect ratio distribution by a lognormal distribution, and consider this in the model, see Fig. A.9 in Appendix A. Unfortunately, only one dataset (#29) was found that contains chemical information on the used fiber [21]; as for the others, we had to rely on typical ranges reported in the literature, as discussed in Section 2.4. Fiber orientations are either set to random (resulting in isotropic composites) for composites #1–29 from Refs. [21,91,99,101–104], (predominantly) aligned along a plane obtained for #106–124 from Refs. [62,99,100], and (predominantly) aligned along an axis for #150–185 obtained from Refs. [63,65,92–98], This is achieved by specification of the orientation distribution function f_o, see the mathematical details in Appendix B. As for fibers aligned along a plane (#106–124), the (spherical) von Mises (vMs) distribution is considered with concentration parameter $\kappa = 10$. This takes into account production-induced deviations of a perfect 2D fiber orientation distribution. As for fibers aligned along an axis, the von Mises-Fisher (vMF) distribution, again with concentration parameter $\kappa = 10$, is adopted in cases where fibers are laid out by hand, or microstructural observation showed imperfect fiber alignments. If prefabricated tapes or cloths with virtually parallel fibers are used, the model also considers perfect fiber alignment. Lumen porosities are measured by some authors [63,92] (data #150–158), but mostly had to be taken from the database collected in [19]. Fiber volume fractions range from 13% to 70%. If only mass fractions are reported, volume fractions are obtained from the fiber and matrix density which were either reported in the papers or obtained from the chemical fiber composition according

Table 3
Reported geometric properties of fibers minimum/**average**/maximum are given: microfibril angle, fiber length, fiber diameter, and calculated aspect ratio; note that the microfibril angles related to minima and maxima stiffness properties may interchange.

Name	Type	Microfibril angle		Fiber length		Fiber diameter		Aspect ratio
		θ [°]	Ref.	l [mm]	Ref.	d [μm]	Ref.	$a = l/d$ [–]
Banana	B	11/**11**/12	[66,67]	0.9/**2.5**/4	[66]	80/**165**/250	[68]	4/**15**/50
Flax	B	5/**10**/10	[1,66]	10/**30**/65	[66,69]	5/**22**/38	[69]	263/**1395**/13 000
Hemp	B	6/**6**/10	[1,66,70]	5/**11.2**/55	[66,69]	10/**22**/51	[66,69]	98/**509**/5500
Isora	B	20/**23**/26	[71]	–/**1**/–	[71]	–/**10**/–	[71]	81/**99**/121
Jute	B	7/**8**/9	[1,66,70]	0.8/**3**/6	[66,69]	5/**15**/25	[66,69]	32/**200**/1200
Kenaf	B	9/**12**/15	[70,72]	1.4/**2.5**/11	[66,69]	12/**20**/36	[66,69]	39/**125**/917
Ramie	B	6/**8**/10	[70]	40/**145**/250	[66,69]	18/**49**/80	[69]	500/**2959**/13 889
Sorghum	B	16/**16**/17	[73]	0.8/**1**/1.2	[68]	30/**55**/80	[68]	10/**18**/40
Alfa	G	–/**10**/–	*	–/**1.9**/–	[67]	–/**13**/–	[67]	120/**146**/179
Bagasse	G	14/**15**/15	[67]	0.8/**1.5**/2.8	[67,69,74]	10/**22**/34	[66,67,69]	24/**68**/280
Bamboo	G	2/**6**/10	[70]	1.3/**2.7**/6.2	[66,67,75,76]	6/**23**/40	[66,75,76]	33/**117**/1033
Abaca	L	–/**23**/–	[67]	4.6/**4.9**/5.2		17/**19**/21		215/**255**/306
Curaua	L	15/**17**/19	[77]	–/**20**/–	[77]	–/**46**/–	[77]	356/**435**/531
Henequen	L	18/**20**/22	[70]	0.5/**0.8**/1.1	[21]	3/**4**/5	[69]	106/**208**/367
Phormium	L	–/**10**/–	*	5/**5.4**/5.7	[66]	15/**16**/16	[66]	305/**336**/370
Pineapple	L	6/**12**/14	[1,66,67]	3/**6**/9	[68,69]	8/**30**/80	[66,69]	38/**200**/1125
Sisal	L	10/**20**/25	[1,66,67]	0.8/**3**/8	[66,69]	7/**27**/47	[66,69]	17/**111**/1143
Coir	F	30/**45**/49	[1,66,70]	0.3/**1.5**/20	[66–69]	7/**18**/30	[66,69]	10/**83**/2857
Cotton	F	20/**25**/30	[66]	15/**39.5**/64	[66,69]	12/**17**/35	[66,69]	429/**2324**/5565
Kapok	F	–/**10**/–	*	10/**22.5**/35	[75]	20/**32**/43	[75]	233/**714**/1750
Oil Palm	F	–/**46**/–	[67]	–/**6**/–	[67]	15/**28**/40	[67]	135/**218**/440
Barley	S	–/**10**/–	*	0.7/**1.9**/3.1	[68]	7/**16**/24	[68]	29/**123**/443
Cornhusk	S	–/**10**/–	*	0.5/**1**/1.5	[68]	10/**15**/20	[68]	25/**67**/150
Cornstalk	S	–/**11**/–	[78]	–/**1**/–	[74]	–/**16**/–	[74]	52/**64**/78
Rice	S	–/**10**/–	*	0.4/**2**/3.5	[67,68]	4/**10**/16	[67,68]	25/**200**/870
Soybean	S	–/**12**/–	[67]	1/**1.5**/2	[79]	12/**16**/19	[79]	52/**96**/167
Wheat	S	–/**0**/–	[80]	–/**1.5**/–	[67]	–/**15**/–	[67]	82/**100**/122

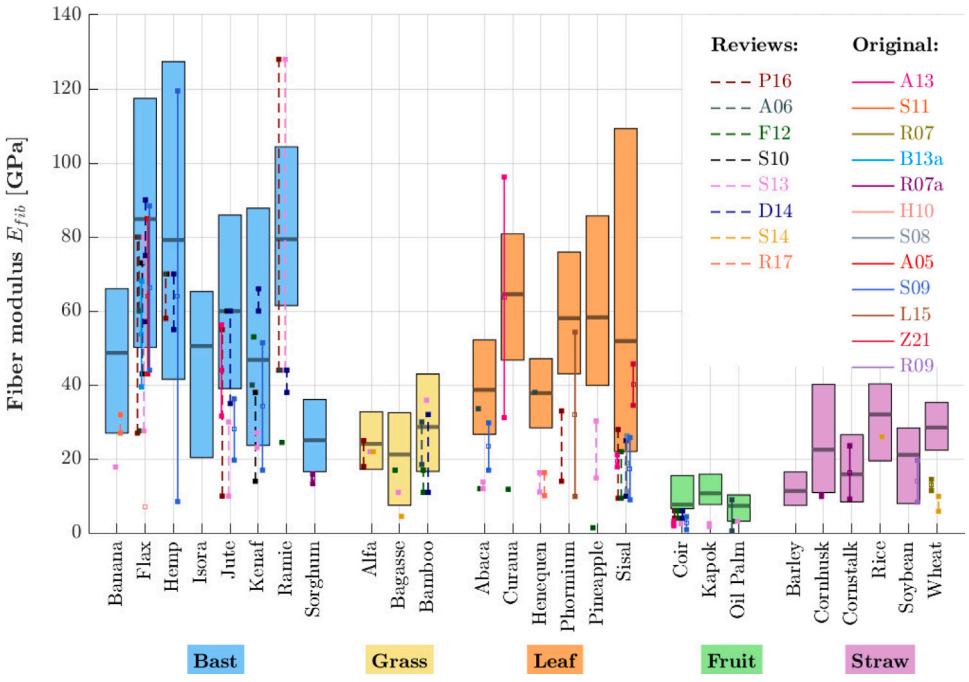

Fig. 2. Validation at the fiber scale: comparison of axial elastic modulus from model predictions (colored bars represent predicted intervals between the minima and maxima modulus, black horizontal lines represent representative averages) with experimental data gathered from published reviews (P16→[3], A06→[70], F12→[81], S10→[82], S13→[7], D14→[2], S14→[83], R17→[84]; dashed lines) and from original tests (A13→[5], S11→[6], R07→[72], B13a→[22], R07a→[73], H10→[85], S08→[86], A05→[87], S09→[88], L15→[63], Z21→[89]; continuous lines); adapted after Königsberger et al. [19].

to Königsberger et al. [19] and from polymer databases (see Table 1). The macropore volume is set to zero if nothing is reported. As for the studies that quantify this porosity [63,97] (data #150–155,181–182), macroporosity is included in the model. Notably, the authors report values up to 13% for high fiber volume fractions, corroborating the trends reported by Madsen et al. [24,25]. The dataset includes an extensive array of matrix materials, including biodegradable polymers such as polypropylene (PP) or polylactic acid (PLA), but also resins and epoxy, see Table D.4. Young's moduli of the matrix material alone (without fibers) were typically tested and thus implemented in the model. Poisson's ratios (and Young's moduli if not reported) were gathered from polymer databases, see Table 1.

Composite Young's moduli were typically tested according to ISO 527 in static tensile tests at room temperature and typically at

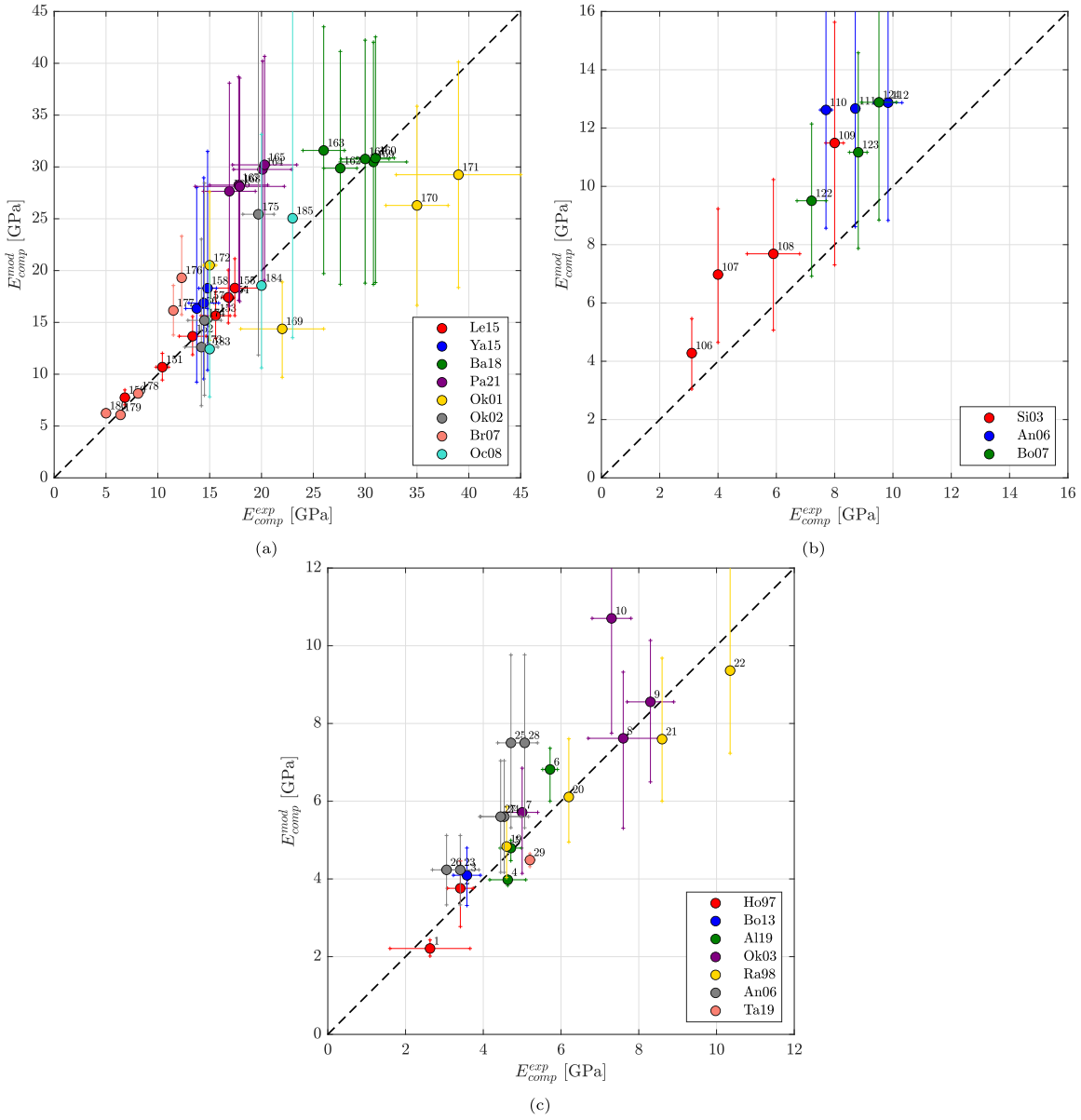

Fig. 3. Validation of composite stiffness for perfect bond: comparison of elastic modulus E_{mod} from model predictions on the vertical axis (points represent means, vertical error bars indicate the max/min; using variations described in the model input Section 2.4) with published experimental counterparts E_{exp} (horizontal error bars indicate standard deviation, if provided) (a) longitudinal modulus for composites with fibers predominantly aligned along an axis (experiments: Le15→[63], Yan15→[92], Ba18→[65], Pa21→[93], Ok01→[94], Ok02→[95], Br07→[96], Gr11→[97], Oc08→[98]); (b) in-plane modulus for composites with fibers predominantly aligned along a plane (experiments: Si03→[62], An06→[99], Bo07→[100]); (c) isotropic modulus for composites with virtually randomly oriented fibers (experiments: Ho97→[101], Bo13→[91], Al19→[102], Ok03→[103], Ra98→[104], An06→[99], Ta19→[21], Oc08→[98]). (For interpretation of the references to color in this figure legend, the reader is referred to the web version of this article.)

50% RH. Tests were typically performed in fiber direction or in the fiber plane. Brahim and Cheikh [96] (data #176–180) also tested at angles ranging from 0 to 90° between fibers and load. Notably, if standard deviations were reported in addition to mean values of the measured Young's modulus, horizontal error bars were included in the comparison plots in Fig. 3. To compare, the model is evaluated for all 73 composites and three cases (minimum/maximum/representative average according to the varying fiber properties, see Section 2.4). This results in representative averages, and a minimum/maximum of model-predicted Young's moduli, which are presented by vertical error bars in the comparison plots in Fig. 3.

Comparing the model predictions with the experimental results reveals the remarkable predictive capabilities of the model. Model results are close to almost all of the experimental data, both if very stiff fibers such as flax (see e.g. #159–163) are aligned leading to very stiff biocomposites with Young's modulus of roughly 30 GPa, but also if relatively soft fibers from wheat straw are randomly put in a polymer matrix (see composite #1) leading to stiffnesses of only 2 GPa. Moreover, the stiffening effect when increasing the fiber content is nicely predicted, for instance the increase of the Young's modulus from composition #150 with 12% of phormium fibers to composition #155 with 50% fiber volume [red dots in Fig. 3(a)]. To further highlight the agreement, this dataset is separately plotted as function of the fiber volume fraction, see Fig. 4. Similarly, the stiffness increase from #19 to #22 [yellow dots in Fig. 3(c)], or even the increase from #106 to #109 [red dots in Fig. 3(b)] is nicely captured, even if the representative average of the model is slightly above the experimental mean. Some mismatches may be explainable, e.g. the overestimated stiffness

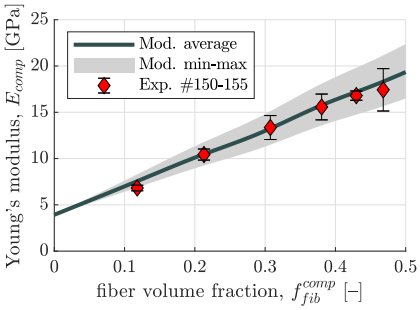

Fig. 4. Longitudinal Young's modulus for perfectly bonded Phormium-epoxy composites tested by Le and Pickering [63] as a function of the fiber volume fraction using a representative average of physical fiber properties (central thick line) and minimum/maximum fiber properties (gray area).

of Pantaloni et al. [93] (#164–168) may be explained by the fact that the flax tapes contain pectin as a coupling agent to stick the individual fibers together but may actually lead to internal imperfect interfaces around or within the tape. Some others may be related to experimental challenges, particularly with high fiber dosages. For instance, the experimentally determined modulus of the flax-PLA composite #10 is smaller than that of #9, despite the latter containing fewer fibers, and despite the fact that the same study reports a significant increase for the flax-PP composites (#7–8) when increasing the fiber volume fraction, which the model very nicely captures.

3.2.3. Imperfect bond

Next, we tackle the comparison of model predictions with experimental results in which severe debonding is either observed by the experimenters or it is considered as an explanation for unexpectedly low mechanical properties. We rely on the experimental data from Devi et al. [106] [#11–18 in Table D.4], Bodros et al. [100] [#116–121], Lu and Oza [107] [#100–105], and Laranjeira et al. [108] [#186–190]. In all those studies, the experimenters report on visible interfacial debonding, or at least speculate that weak interfaces are responsible for the unexpectedly low mechanical properties. Unfortunately, reliable experimental access to the interface compliance in biocomposites is still very limited. As a remedy, the interface compliance was calibrated. Most notably, we considered that the interface compliance only depends on the fiber and the matrix material, but does not depend on the fiber volume fraction or the fiber length. Moreover, we consider – for simplicity – that the tangential and normal interface compliance are identical, $\alpha = \beta$.

After fitting the (normalized) interface compliances $\overline{\alpha} = \overline{\beta}$, model predictions considering imperfect bond (continuous lines in Fig. 5) nicely agree with the experimental results, both for different fiber volume fractions as well as for different fiber lengths. Perfect bond-related model predictions (dashed lines) significantly overestimate the stiffness. The fitted interface compliance values range from $\overline{\alpha} = \overline{\beta} = 4.3$ m/MPa for PLA-flax composites (Exp.#117–119) to 2680 m/MPa for polyester-jute composites showing very weak bonding (Exp.#186–190). Three remarkable observations from the comparison between model and experiment are further discussed next.

Firstly, the experiments from Lu and Oza [107] are discussed. The experimenters probe the longitudinal Young's modulus of a hemp-HDPE composite with fibers and increase the fiber volume fraction from 20% to 40%. Model prediction can match the experimental results only if nonzero interface compliances are considered, while perfect-bond related predictions significantly overestimate the tested modulus. Fitting of the interface compliance leads to $\overline{\alpha} = \overline{\beta} = 37.3$/MPa and a very nice agreement of model and experiment, see Fig. 5(a). By analogy, Bodros et al. [100] tested flax-PP and flax-PLA composites with volume fractions of 20, 25, and 30% of fibers, respectively. Slightly weakened interfaces with $\overline{\alpha} = \overline{\beta} \approx 5$/MPa result in model predictions that very closely match the test data, see Fig. 5(d).

Next, the experiments from Devi et al. [106] (#11–18) are analyzed in more detail. The experimenters tested a composite with randomly oriented pineapple leaf fibers in a polyester matrix and increase the fiber mass fraction from 10% to 40% (Exp.#11–14, fiber length $l_f = 30$ mm) and the fiber length from 5 to 30 mm (Exp.#15–18, fiber mass fraction 30%). The imperfect-bond model is capable of predicting the stiffness increase with both the increasing fiber volume fraction, see Fig. 5(b), and the increasing fiber length, see Fig. 5(c). Notably, a single interface compliance was fitted $\overline{\alpha} = \overline{\beta} = 1,870$/MPa to predict all eight composites. A micromechanics model with perfect bonds would not predict a significant benefit with increasing fiber lengths, see the dashed line in Fig. 5(c), given that even for the 5 mm-long fibers, the fiber diameter of 30 μm is more than two orders of magnitude smaller than the fiber length. The sensitivity regarding the aspect ratio is high only when the bond is weak. Notably, the model with fitted interface compliance $\overline{\alpha} = \overline{\beta} = 1,870$/MPa predicts that the Young's modulus does not significantly increase if the fiber length is increased beyond 30 mm. Such threshold lengths have also been observed in experiments on glass fiber composites [109,110], and are further analyzed in the model sensitivity section.

Finally, the experiments from Laranjeira et al. [108] (#186–190) are discussed. The experimenters probed both the longitudinal and transversal Young's modulus of a composite with aligned jute fibers embedded in a polyester matrix and increase the fiber mass fraction from 10% to even 50%. The imperfect-bond model is not only capable of predicting the modest increase of the longitudinal modulus with increasing fiber volume fraction, see Fig. 5(e), but also nicely predicts the decreasing transversal modulus, see Fig. 5(f) – employing an intrinsic interface compliance $\overline{\alpha} = \overline{\beta} = 2,680$/MPa.

4. Model sensitivity

Motivated by the successful model validation, we study the sensitivity of the model-predicted stiffness concerning changes of (i) the fiber volume fraction, (ii) the (constant) fiber aspect ratio, (iii) the fiber aspect ratio distribution, (iv) the fiber orientation distribution, and (v) the fiber–matrix interface stiffness. First, a benchmark composition is defined, based on the tested biocomposite from [22], labeled as #3 in Table D.4. Flax fibers with a volume fraction of $f_{fib}^{comp} = 13.7\%$ are embedded in a polymer matrix made from polypropylene with 4% (by mass) of polypropylene-grafted maleic anhydride (PP-g-MA) acting as a coupling agent. The coupling agent motivates the use of a perfectly bonded interface with interface compliances $\alpha = \beta = 0$. As for the flax fibers, we use the average volume fractions given in Table 2 and the average microfibril angle of 10° given in Table 3. The aspect ratio of all fibers is considered constant and is given in the reference as $\overline{a} = 51.7$, the corresponding aspect ratio distribution is a Dirac delta distribution,

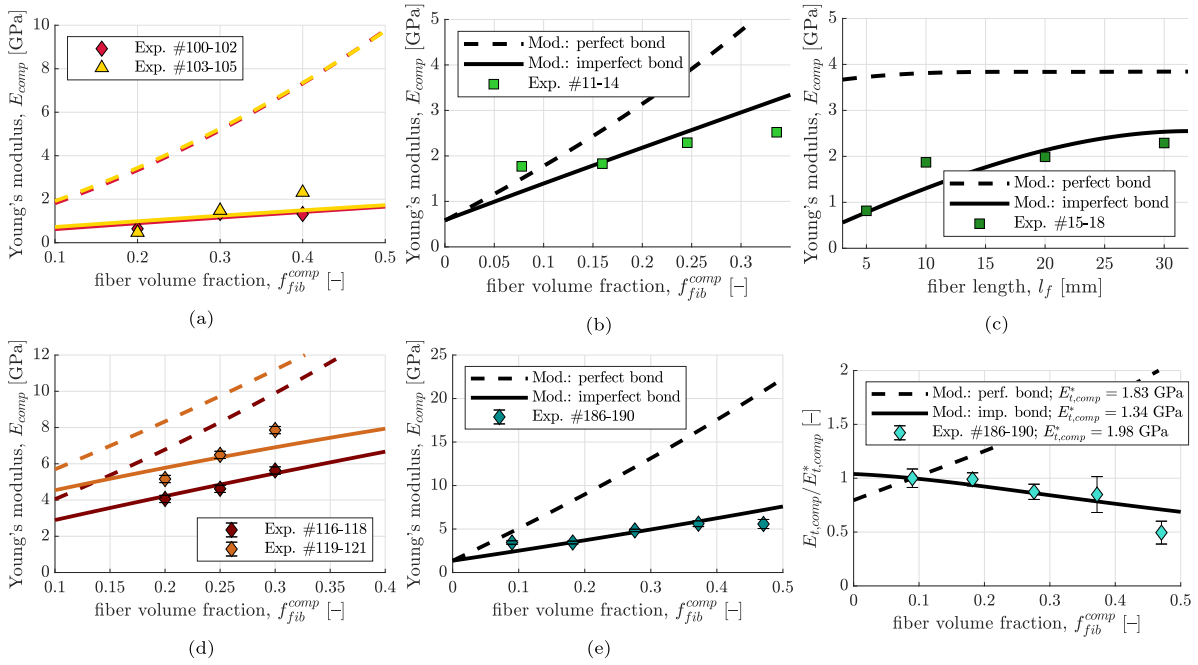

Fig. 5. Validation of composite for imperfect bond: Longitudinal (a-e) and transversal (f) Young's modulus tested by (a) Lu and Oza [107] for HDPE-hemp [Exp.#100–105, $\overline{\alpha} = \overline{\beta}$ = 37.3/MPa], (b-c) Devi et al. [106] for polyester-pineapple leaf fiber (PALF) [Exp.#11–18, $\overline{\alpha} = \overline{\beta}$ = 1870/MPa], (d) Bodros et al. [100] for PP-flax [Exp.#116–118, $\overline{\alpha} = \overline{\beta}$ = 5.3 m/MPa] and PLA-flax [Exp.#117–119, $\overline{\alpha} = \overline{\beta}$ = 4.3/MPa], and (e-f) Laranjeira et al. [108] for polyester-jute [Exp.#186–190, $\overline{\alpha} = \overline{\beta}$ = 2680/MPa] as function of the fiber volume fraction (a–b,d–f) and fiber length (c); imperfect bond model (continuous lines) with fitted interface compliances $\overline{\alpha} = \overline{\beta}$ compared to perfect bond predictions (dashed lines).

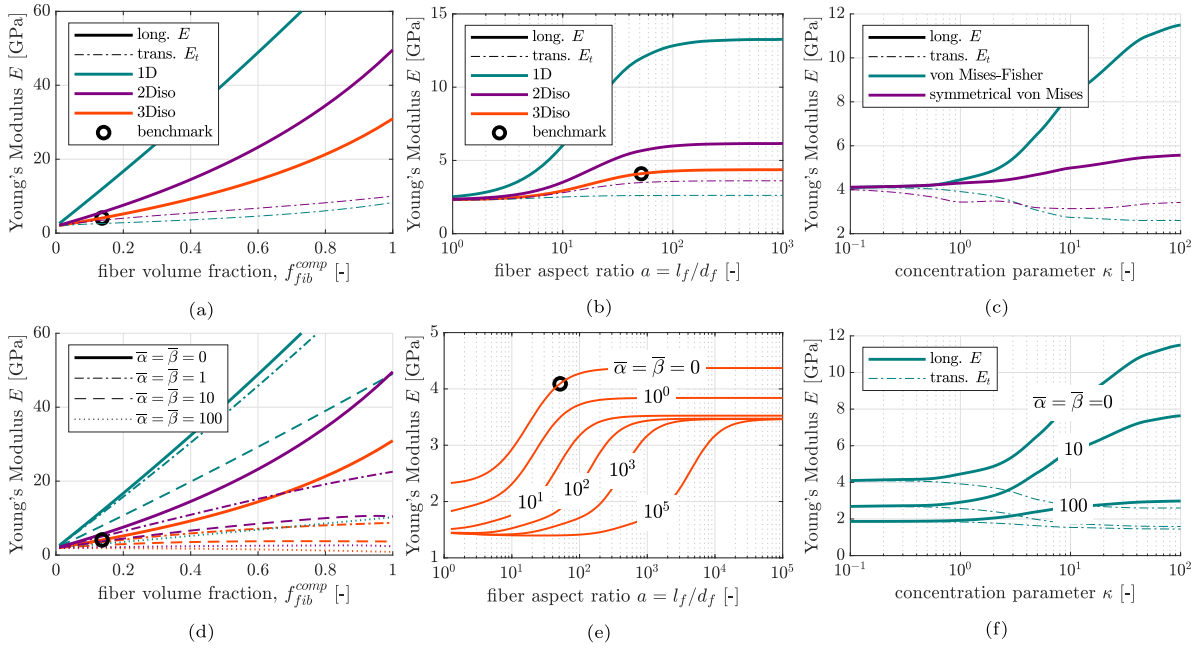

Fig. 6. Sensitivity analyses of the composite's Young's modulus (E ... in plane or longitudinal modulus and E_t ... transversal modulus) based on benchmark composition for perfectly bonded fibers (top row) and imperfectly bonded fibers (with interface compliance $\overline{\alpha} = \overline{\beta}$ with unit [1/GPa], bottom row) and with different fiber orientations (1D ... aligned, 2Diso ... isotropically oriented in a plane, 3Diso ... isotropic in all directions): (a)+(d) w.r.t fiber volume fraction (b)+(e) w.r.t. the fiber aspect ratio, (c)+(f) w.r.t. concentration parameter of von Mises Fisher and (symmetrical) von Mises distribution function; note that (e) is limited to 3Diso orientations and (f) to von Mises-Fisher distribution; black circle refers to the benchmark composition.

$f_a(a) = \delta\left(a - \overline{a}\right)$, see (A.1) in Appendix A. The fiber orientation is considered to be uniform in all space directions, $f_o = \frac{1}{4\pi}$, see (B.1) in Appendix B. In the following paragraphs, we consecutively vary several parameters to study their effect on the composite stiffness.

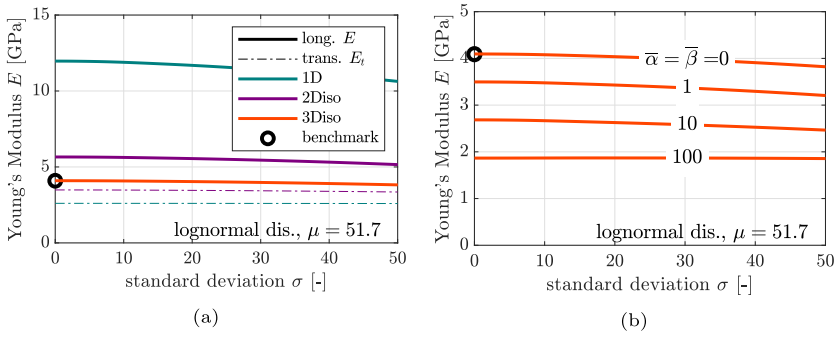

Fig. 7. Sensitivity analyses of the composite's Young's modulus based on benchmark composition w.r.t. fiber aspect ratio distribution considering lognormal distributions with constant mean $\mu = 51.7$ but varying standard deviations ranging from $\sigma = 0$ (Dirac distribution) to $\sigma = 50$: (a) perfect bond for different fiber orientations (1D ... aligned, 2Diso ... isotropically oriented in a plane, 3Diso ... isotropic in all directions) (b) imperfect bond for 3Diso composites with interface compliance $\overline{\alpha} = \overline{\beta}$.

Increasing the *fiber volume fraction* significantly increases the stiffness if the interface is relatively strong, see Fig. 6(a,d). The longitudinal Young's modulus (solid lines) is obviously higher if fibers are aligned along an axis (1Diso) and the transversal modulus is obviously smaller, respectively, in comparison to fibers aligned along a plane (2Diso). The Young's modulus for an isotropic composite with randomly oriented and perfectly bonded fibers increases from 1.89 GPa at vanishing fiber volume ($f_{fib}^{comp} = 0$) to 30.94 GPa for the theoretical limit case of vanishing matrix material ($f_{fib}^{comp} = 1$), see Fig. 6(a). If the interface between fiber and matrix gets weaker (the compliance $\overline{\alpha} = \overline{\beta}$ increases), the stiffening effect is less pronounced. For weak interfaces, there may even be a softening effect, i.e., increasing the fiber volume leads to decreasing stiffness, just as observed and predicted for the jute-polyester composite tested by Laranjeira et al. [108] shown in Fig. 5(e-f). Studying the mutual influence of the interface compliance and orientation distribution with respect to the fiber volume fraction, see Fig. 6(d), we notice that slightly imperfect interfaces with $\overline{\alpha} = \overline{\beta} = 1$ reduce the stiffness of composites with axis-aligned fibers (1Diso) only marginally, but have a more significant impact on plane-aligned fibers (2Diso), and a dramatic reduction effect on isotropically oriented fibers (3Diso).

Increasing the *fiber aspect ratio* (elongating the fibers while maintaining a constant diameter) results in composite stiffening, see Fig. 6(b). The (isotropic) modulus for the theoretical case of spherical fibers ($a = 1$) amounts to 2.3 GPa. The modulus increases in an S-shaped fashion when plotted on a logarithmic scale. Remarkably, the stiffness remains virtually constant for aspect ratios larger than the threshold of roughly 100, see Fig. 6(b). However, this observation holds only in the case of perfectly bonded fibers. When examining imperfectly bonded fibers, as presented in Fig. 6(e), with interface compliance $\overline{\alpha} = \overline{\beta}$ between zero (perfect bond) and 10^5/GPa (very weak), the S-shaped trend is maintained. The stiffness increase, however, initiates and ends at larger aspect ratios if interfaces are considered weak. We note that threshold aspect ratios beyond which the stiffness does not increase further have been reported from experimental testing on glass fiber composites [109,110]. This is also critical for biocomposites, where typical fiber aspect ratios fall between 5 and 5000 (Table 3), hence precisely in the range in which the interplay between fiber aspect ratio and interface compliance governs the composite stiffness. Interestingly, for interface compliance values exceeding $\overline{\alpha} = \overline{\beta} \geq 10^2$/GPa, the composite stiffness initially even decreases with increasing aspect ratio. This highlights that the benefit of more elongated fibers is reversed in the presence of substantial interface compliance. Despite being smaller than for the benchmark model, the stiffness, even for composites with very weak interfaces, is surprisingly high, provided that the fiber aspect ratio is also very high. We conclude that the interplay between fiber aspect ratio and interface compliance is crucial for quantifying the stiffness of fiber-reinforced composites. If interfaces are weak, fibers have to be more elongated to result in reasonable composite stiffnesses, but increasing the fibers beyond a certain threshold does not further stiffen the composite.

Next, we compare the effect of *fiber orientation distributions* on perfectly [Fig. 6(c)] and imperfectly bonded [Fig. 6(f)] fibers. We employ the von Mises-Fisher distribution for fibers that concentrate along an axis and the von Mises distribution for fibers that are concentrated in a plane. Appendix B details the orientation distributions, including their density functions, and visualizes the orientations on a unit sphere. Both orientation distributions exhibit a single concentration parameter $\kappa > 0$, where the fibers are randomly oriented if $\kappa \to 0$ and where the alignment (along an axis or a plane, respectively) increases with increasing concentration parameter, see Fig. B.10. Evaluating the multiscale model for different $\kappa \in [0, 10^2]$ shows that increasing the concentration significantly increases the stiffness in the preferred fiber direction, but significantly decreases the stiffness orthogonal to it, see Fig. 6(d). In the limit case $\kappa \to \infty$, the fibers are perfectly aligned with the axis (or plane) the stiffness approaches the results for the 1D orientation distribution (2Diso distribution), discussed earlier. If interfaces are weak, the influence of concentration parameters is smaller, as the fibers contribute less to the load bearing capacity. This is illustrated for composites with fibers preferably oriented along an axis (von Mises-Fisher distribution) in Fig. 6(f). The stiffening effect of the longitudinal modulus and the softening effect on the transversal modulus for such composites is smaller when the interface is more compliant.

Next, the sensitivity of the *aspect ratio distribution* is studied. In contrast to the benchmark, where all fibers exhibit a single constant aspect ratio of $a = 51.7$, we now consider the natural logarithm of the fiber's aspect ratio to be normally distributed. This asymmetric lognormal distribution is a popular choice for natural fibers and confirmed experimentally [23]. In more detail, the mean value of the aspect ratio is kept at $\mu_a = 51.7$, but the standard deviation is considered to vary within the interval $\sigma_a \in [0, 51.7]$. The model-predicted moduli slightly decrease with increasing standard deviation, see Fig. 7(a), because of the asymmetric nature of the lognormal distribution. If interfaces are considered weak, the already small influence of the standard deviation is even smaller, see Fig. 7(b). Note that homogenization based on mean aspect ratios may also lead to significant underestimation of the homogenized stiffness [111].

Finally, we study the results for changes of the *interface compliances* $\overline{\alpha} \neq \overline{\beta}$. The contour-plots depicted in Fig. 8 show the combined effects when changing $\overline{\alpha}$ and $\overline{\beta}$ independently. The predicted stiffness decrease is more pronounced when the tangential compliance $\overline{\alpha}$ increases. Reducing the radial compliance $\overline{\beta}$ by a similar amount leads to a smaller stiffness reduction. To achieve a composite stiffness of 3 GPa with randomly oriented fibers [Fig. 8(a)], the normalized radial compliance can be as high as 330/GPa if the tangential compliance vanishes. In contrast, the normalized tangential compliance (with vanishing radial compliance) can only be increased to roughly 10/GPa to obtain

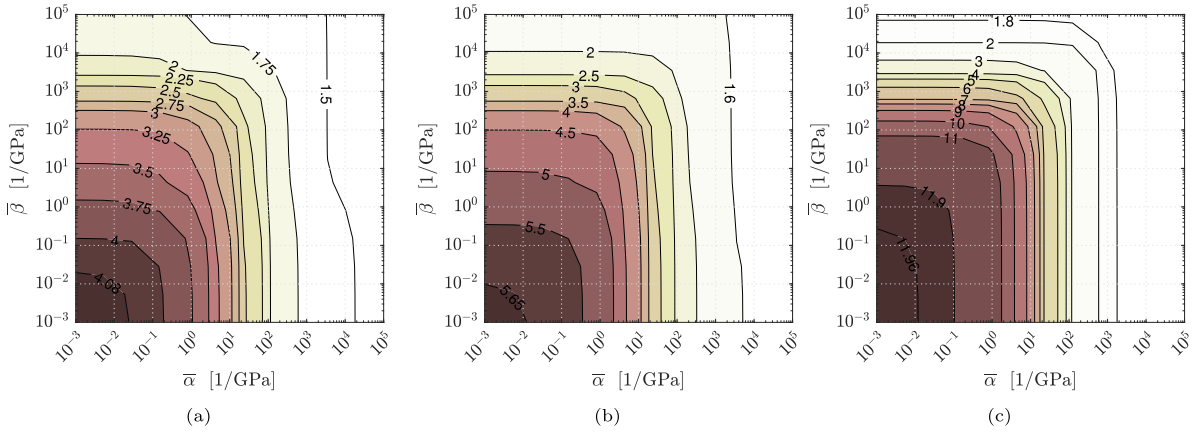

Fig. 8. Sensitivity analyses of the composite's stiffness based on benchmark composition w.r.t. interface compliances: (a) isotropic Young's modulus for randomly oriented fibers (b) in-plane modulus for plane-aligned fibers and (c) longitudinal modulus for axis-aligned fibers.

the same composite stiffness of 3 GPa. Similar observations can be made with fibers distributed randomly in a plane [Fig. 8(b)] and for axis-aligned fibers [Fig. 8(c)]. Comparing the reduction in stiffness concerning the orientation distribution, as illustrated in Fig. 8(a–c), reveals that compliant interfaces have a more pronounced softening effect on composites with a higher degree of fiber alignment, at least in relative terms, when measuring the reduction in stiffness in relation to the composite's stiffness with perfect bonds.

5. Conclusions and outlook

A micromechanics multiscale model for stiffness homogenization of plant fiber-reinforced composites is developed. The model builds up on the intrinsic elastic properties of cellulose, hemicellulose, and lignin to predict the fiber stiffness and then allows to account for (any) fiber orientation distribution, (any) fiber aspect ratio distribution, and, most importantly, a weak interface between fiber and matrix to predict the composite stiffness. The model is successfully validated by comparing model predictions to experimentally quantified Young's moduli for 73 different composites produced from ten different plants tested in several laboratories over the last two decades. While none of the experiments provide all possible input data, comparisons without fitting any of the input properties are still achievable by relying on typical ranges of physico-chemical fiber properties (such as microfibril angle or cellulose contents) and on single-parameter fiber orientation distributions functions. Challenging the model with such a high quantity and diversity of experiments ensures that the model does indeed incorporate all microstructural aspects that are essential for predicting the elastic behavior of plant fiber-reinforced composites.

Sensitivity studies show that the composite stiffness can be increased by increasing the fiber volume fraction, lowering the interface compliance, aligning the fibers, or elongating the fibers. Studying the interplay between the individual effects reveals several interesting observations. Increasing the fiber length leads to substantial composite stiffening if fibers are short and/or if the interfaces are weak. Increasing the fiber length beyond a certain threshold (the threshold increases with increasing interface compliance) does not further stiffen the composite. Slightly weakening the interfaces leads to substantial softening of composites with more uniformly distributed fiber orientations, while composites with more alignment are less affected.

In the future, the model will be extended towards the prediction other physical properties of plant fiber-reinforced composites, including thermal conductivity and viscoelasticity. Moreover, we target the composite failure prediction by linking the analytical model presented herein with a numerical approach incorporating the major microscopic failure modes such as matrix softening and interface failure. This model also provides motivation for experimenters to improve the characterization techniques for two very crucial aspects that determine the mechanical properties of biocomposites, namely the quantification of the fiber orientation distribution and the interface properties.

CRediT authorship contribution statement

Markus Königsberger: Writing – original draft, Visualization, Software, Methodology. **Valentin Senk:** Investigation. **Markus Lukacevic:** Writing – review & editing, Funding acquisition. **Michael Wimmer:** Writing – review & editing, Funding acquisition. **Josef Füssl:** Funding acquisition, Conceptualization.

Declaration of competing interest

The authors declare that they have no known competing financial interests or personal relationships that could have appeared to influence the work reported in this paper.

Data availability

No data was used for the research described in the article.

Acknowledgments

The authors gratefully acknowledge the financial support by the Austrian Science Fund (FWF) through the SFB F77 project and the START project Y1093-N30. Furthermore, financial support from the Austrian Federal Ministry of Labour and Economy, the National Foundation for Research, Technology and Development, Austria, and the Christian Doppler Research Association is gratefully acknowledged.

Appendix A. Aspect ratio distribution

Herein, we discuss the distribution function f_a of the aspect ratio $a = l_f/d_f$ (Fig. 1) to quantify the geometry of the spheroidal fiber with length l_f and diameter d_f. Notably, aspect ratios $a = 1$ characterize spherical phases, and aspect ratios $a \to \infty$ represent cylindrical phases. Generally, aspect ratios of a phase are continuously distributed within the interval $a \in [0, \infty]$. The probability density function of the distribution is given by the aspect ratio density function $f_a(a)$, where $\int_0^\infty f_a(a)\,\mathrm{d}a = 1$. Three often used aspect ratio density functions to characterize fiber-reinforced composites are discussed next.

If all fibers in the composite exhibit identical aspect ratio $\overline{a}$, the *uniform* aspect ratio distribution can be given as

$$f_a(a, \overline{a}) = \delta\left(a - \overline{a}\right) \tag{A.1}$$

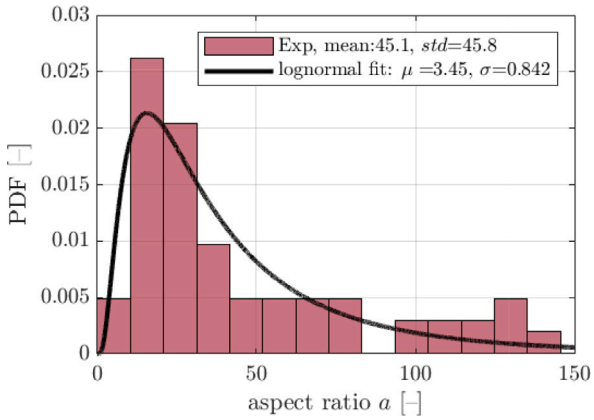

Fig. A.9. Experimentally measured histogram for aspect ratios of flax fibers from [22] and lognormal fit according to (A.3).

where $\delta(.)$ denotes the Dirac delta function. According to Moigne et al. [23], aspect ratio distribution for several natural fibers can be successfully fitted using a *Weibull* distribution or a *lognormal distribution*. The probability density function of a Weibull distribution reads as

$$f_a(a,\lambda,k) = \begin{cases} \frac{k}{\lambda}\left(\frac{a}{\lambda}\right)^{k-1} \exp\left[-\left(\frac{a}{\lambda}\right)^{k}\right] & x \geq 0 \\ 0 & x < 0 \end{cases} \tag{A.2}$$

with shape parameter $k > 0$ and scale parameter $\lambda > 0$. Notably, typical values for k and λ, for flax-PP composites read as $k = 1.9$ and $\lambda = 10.2$, for sisal-PP composites as $k = 2.0$ and $\lambda = 5.9$, and for wheat straw-PP composites as $k = 1.5$ and $\lambda = 2.5$, see Moigne et al. [23]. The probability density function of a lognormal distribution, in turn, reads as

$$f_a(a,\mu,\sigma) = \frac{1}{a\sigma\sqrt{2\pi}} \exp\left[-\frac{(\ln a - \mu)^2}{2\sigma^2}\right], \tag{A.3}$$

with μ and σ as the mean value and standard deviation, respectively, of the aspect ratios natural logarithm. The lognormal distribution was also used to fit the aspect ratio histogram provided by Bourmaud et al. [22] for a flax-PP composite.

As for stiffness homogenization, the continuous aspect ratio distribution function is discretized using $M = 20$ bins of equal probability. This way, integration of the (tensorial) property $P(a)$ with continuous aspect ratio distribution function $f(a)$ is approximated as

$$\int_0^\infty f_a(a)\, P(a)\, \mathrm{d}a = \sum_{i=1}^{M} f_a(p_i) P(a_i) \tag{A.4}$$

with p_i denoting the quantile values, which are determined by evaluating the quantile function (inverse cumulative distribution) for $M = 20$ equidistant probabilities $p_i = \{0.025, 0.075, 0.125, \ldots, 0.975\}$. This way, the RVE biocomposite is composed of 20 fiber families with equal volume fractions, where each family exhibits the orientation distribution function f_o.

Appendix B. Fiber orientation distribution

A single fiber's orientation is defined by zenith angle ϑ and azimuth angle φ, see Fig. 1. In more detail, the zenith angle is the angle between the macroscopic direction z and the fiber axis L. The azimuth angle, in turn, is the angle in the macroscopic x, y-plane between the fiber-related direction R and the macroscopic x direction. Orientations of multiple fibers are characterized by a normalized probability density (orientation distribution) function $f_o(\vartheta, \varphi)$, where the integral along all possible directions on the surface of the unit sphere is one, $\int_0^{2\pi}\int_0^{\pi} f_o \sin(\vartheta)/4\pi \,\mathrm{d}\vartheta\mathrm{d}\varphi = 1$.

As for isotropically oriented fibers in all space directions, the orientation distribution function reads as

$$f_o^{\mathrm{3Diso}} = \frac{1}{4\pi} \tag{B.1}$$

As for fibers isotropically oriented in a plane perpendicular to unit vector $\underline{m}$, the orientation distribution function reads as

$$f_o^{\mathrm{2Diso}} = \frac{1}{2\pi}\delta\left(\underline{m}\cdot\underline{n}\right) \tag{B.2}$$

where $\delta(.)$ denotes the Dirac delta function, with $\underline{m}$ denoting the modal vector where herein $\underline{m} = \underline{e}_z$, and with $\underline{n} = [\cos(\varphi)\sin(\vartheta), \sin(\varphi)\sin(\vartheta), \cos(\vartheta)]^T$ denoting a generic vector on the unit sphere defined based on azimuth angle φ and zenith angle ϑ. If all fibers are aligned with $\underline{m}$, the orientation distribution function reads as

$$f_o^{\mathrm{align}} = \frac{\delta\left(1-\left(\underline{m}\cdot\underline{n}\right)^2\right)}{4\pi\sqrt{1-\left(\underline{m}\cdot\underline{n}\right)^2}} \tag{B.3}$$

To account for fibers that are preferably (but not exclusively) oriented along an axis $\underline{m}$ orientation, e.g. due to a composite extrusion [22], we consider the transversally isotropic "von Mises-Fisher" distribution, reading as [112]

$$f_o^{\mathrm{vMF}} = \frac{\kappa}{4\pi\,\sinh\kappa}\exp\left(\kappa\underline{m}\cdot\underline{n}\right) \tag{B.4}$$

with $\kappa \geq 0$ denoting the concentration parameter. Notably, for fibers oriented in all space directions isotropically, the concentration parameter κ in (B.4) vanishes, such that the orientation distribution function simplifies to the form (B.1). With increasing concentration parameter κ, the fibers become more and more aligned (with modal vector $\underline{m}$), see Fig. B.10(a–d), with the limit case given by Eq. (B.3).

Finally, we consider another rotationally symmetric fiber orientation distribution where fibers are preferably (but not exclusively) oriented along the $\underline{e}_1, \underline{e}_2$. Such orientation distributions represent composites manufactured by the popular film-stacking method either with prefabricated fiber mats (with in-plane isotropy) or by randomly hand-laying fibers. For the derivation of the corresponding probability density function, we start with the (circular) "von Mises" distribution, with probability density function $g^{\mathrm{vM}}(\vartheta)$ as a function of the zenith angle ϑ, reading as [112]

$$g^{\mathrm{vM}} = \frac{a}{2\pi\, I_0(\kappa)}\exp\left[\kappa\,\cos\left(\vartheta-\frac{\pi}{2}\right)\right] \tag{B.5}$$

with κ as the concentration parameter and I_0 as the modified Bessel function of the first kind and with order 0. The corresponding spherical distribution f_o^{vMs} results from normalization and reads as

$$f_o^{\mathrm{vMs}} = \frac{g_o^{\mathrm{vM}}}{\int_0^{2\pi}\int_0^{\pi} g_o^{\mathrm{vM}}\frac{\sin(\vartheta)}{4\pi}\,\mathrm{d}\vartheta\mathrm{d}\varphi} \tag{B.6}$$

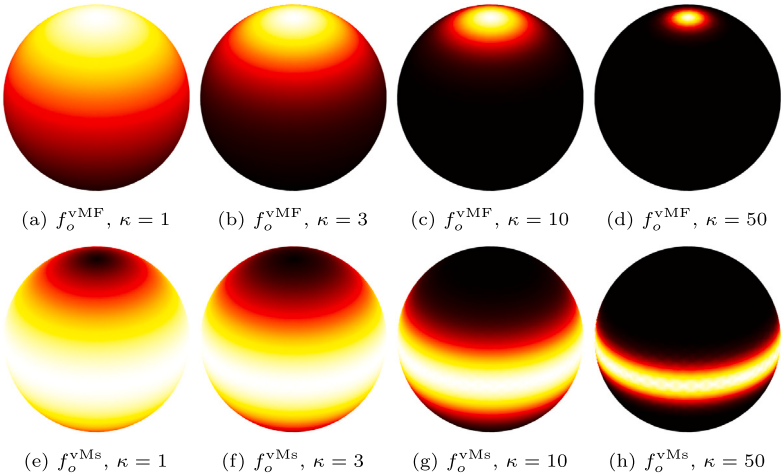

(a) f_o^{vMF}, $\kappa = 1$ (b) f_o^{vMF}, $\kappa = 3$ (c) f_o^{vMF}, $\kappa = 10$ (d) f_o^{vMF}, $\kappa = 50$

(e) f_o^{vMs}, $\kappa = 1$ (f) f_o^{vMs}, $\kappa = 3$ (g) f_o^{vMs}, $\kappa = 10$ (h) f_o^{vMs}, $\kappa = 50$

Fig. B.10. Orientation distribution functions $f_o(\vartheta, \varphi)$, where $\int_0^\infty f_o(\vartheta, \varphi) \sin\vartheta \, \mathrm{d}\vartheta \, \mathrm{d}\varphi = 1$, plotted on the unit sphere (the darker, the smaller is f_o): (a–d) "von Mises-Fisher" distribution with modal vector $\underline{m}$ along the vertical direction (e–h); and "von Mises" distribution evaluated for different concentrations κ.

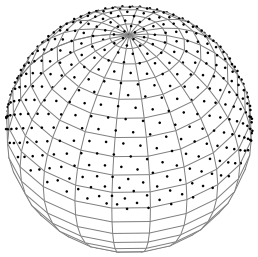

Fig. B.11. Unit sphere with Lebedev quadrature visualized for $N = 974$ points in the top hemisphere for the discretization of the antipodal symmetric "von Mises" orientation distribution function f_o^{vMs}.

As for stiffness homogenization, the continuous orientation distribution function is discretized using up to $N = 5810$ orientations determined by the Lebedev quadrature points [113]. High values of N are necessary for very anisotropic orientation distributions, such as "von Mises-Fisher" distribution with high concentration factors κ. Exploiting the antipodal symmetry of the "von Mises" distribution functions f_o^{vMs} with respect to the x, y plane (zenith angle $\vartheta = \pi/2$), only points in the top hemisphere are actually considered, as depicted in Fig. B.11. However, the "von Mises-Fisher" distribution f_o^{vMF} does not exhibit antipodal symmetry, requiring the evaluation at quadrature points along the whole sphere. This way, surface integration of the (tensorial) property $P(\varphi, \vartheta)$ with fiber orientation distribution function $f(\varphi, \vartheta)$ over the hemisphere is approximated as

$$\int_0^{\pi/2} \int_0^{2\pi} f_o(\varphi, \vartheta)\, P(\varphi, \vartheta) \sin\theta \, \mathrm{d}\varphi \, \mathrm{d}\vartheta = 4\pi \sum_{i=1}^{N} w_i f_o(\varphi_i, \vartheta_i) P(\varphi_i, \vartheta_i) \quad \text{(B.7)}$$

with grid points (φ_i, ϑ_i) and weights w_i according to Lebedev [113]. Orientations for which $f_o(\varphi_i, \vartheta_i) \leq 10^{-5}$ are disregarded.

Appendix C. Analytical formulae for stiffness homogenization

Herein we provide full mathematical details regarding the bottom-up stiffness homogenization for the biocomposite model depicted in Fig. 1. The homogenized stiffness of the polymer network $\mathbb{C}_{pn}$ follows from specialization of homogenization rule (12) for $N = 5$ spherical and isotropic phases hemicellulose, lignin, pectin, wax, and ash, with perfectly bonded interfaces (resulting in $\mathbb{R}_{i/0} = 0$). This way, self-consistent homogenization ($\mathbb{C}_0 = C_{pn}$) yields

$$\mathbb{C}_{pn} = \left\{ \sum_i f_i^{pn} \mathbb{C}_i : \left[\mathbb{I} + \mathbb{S}_{sph}^{pn} : \mathbb{C}_{pn}^{-1} : \left(\mathbb{C}_i - \mathbb{C}_{pn} \right) \right]^{-1} \right\}$$

$$: \left\{ \sum_j f_j^{pn} \left[\mathbb{I} + \mathbb{S}_{sph}^{pn} : \mathbb{C}_{pn}^{-1} : \left(\mathbb{C}_i - \mathbb{C}_{pn} \right) \right]^{-1} \right\}^{-1} \quad \text{(C.1)}$$

with $i, j \in \{\text{hemcel,lig,pec,wax,ash}\}$ and $\mathbb{S}_{sph}^{pn}$ as the Eshelby tensor of spherical phases in an infinite matrix of polymer network, given at the end of this section. The homogenized stiffness of the cellulose microfibril $\mathbb{C}_{celMF}$ follows from specialization of homogenization rule (12) for $N = 2$ phases, namely cylindrical ($a \to \infty$) and aligned (orientation distribution according to Eq. Appendix B) crystalline cellulose perfectly bonded to the amorphous cellulose matrix. This way, Mori–Tanaka homogenization ($\mathbb{C}_0 = C_{amcel}$) yields

$$\mathbb{C}_{celMF} = \left\{ f_{amcel}^{cel} \mathbb{C}_{amcel} : \mathbb{I} + f_{crycel}^{cel} \mathbb{C}_{crycel} : \left[\mathbb{I} + \mathbb{S}_{cyl}^{amcel} : \mathbb{C}_{amcel}^{-1} : \left(\mathbb{C}_{crycel} - \mathbb{C}_{amcel} \right) \right]^{-1} \right\} :$$

$$\left\{ f_{amcel}^{cel} \mathbb{I} + f_{crycel}^{cel} \left[\mathbb{I} + \mathbb{S}_{cyl}^{amcel} : \mathbb{C}_{amcel}^{-1} : \left(\mathbb{C}_{crycel} - \mathbb{C}_{amcel} \right) \right]^{-1} \right\}^{-1} \quad \text{(C.2)}$$

with Eshelby tensor components of $\mathbb{S}_{cyl}^{amcel}$ given at the end of this section. Notably, asymmetries related to Mori–Tanaka homogenization with anisotropic phases [114] are symmetrized [115]. The homogenized stiffness of the cell wall $\mathbb{C}_{cw}$ follows from specialization of homogenization rule (12) for $N = 2$ phases, namely cylindrical ($a \to \infty$) cellulose microfibrils with transversally isotropic stiffness according to Eq. (C.2), perfectly bonded to a polymer network matrix with isotropic stiffness according to Eq. (C.1). Given the microfibril orientation with constant microfibril angle $\bar{\vartheta} \geq 0$ but uniform orientation along the azimuth φ, the surface integration in Eq. (13) is replaced by integration along the circumference. Mori–Tanaka homogenization ($\mathbb{C}_0 = C_{pn}$) yields

Table D.4
Experimental data for model validation. Missing data are not given by experimenters (empty cells). Instead, they are obtained from standard literature data for fibers from Table 3 and matrix materials from Table 1. Fiber–matrix bond (last column) is considered perfect (✓) except if stated otherwise in the experimental paper (✗). Then, the interface compliance parameters $\overline{\alpha} = \overline{\beta}$ are fitted.

#	Ref	Fiber	ρ_{fib} [g/cm^3]	l_f [mm]	d_f [μm]	FibOri	f_{fib}^{comp}	Matrix	ρ_{mat} [g/cm^3]	E_{mat} [GPa]	Bond
1	[101]	Wheat				3Diso	0.168	PP		1.18	✓
2	[101]	Flax	1.54			3Diso	0.135	PP		1.18	✓
3	[22]	Flax				3Diso	0.137	PP		1.89	✓
4	[102]	Flax	1.5	1	125	3Diso	0.084	PLA	1.24	3.26	✓
5	[102]	Flax	1.5	1	125	3Diso	0.171	PLA	1.24	3.26	✓
6	[102]	Flax	1.5	1	125	3Diso	0.355	PLA	1.24	3.26	✓
7	[103]	Flax	1.5			3Diso	0.205	PP	0.9	1.6	✓
8	[103]	Flax	1.5			3Diso	0.286	PP	0.9	1.6	✓
9	[103]	Flax	1.5			3Diso	0.265	PLA	1.26	3.4	✓
10	[103]	Flax	1.5			3Diso	0.359	PLA	1.26	3.4	✓
11	[106]	Pineapple	1.53	30		3Diso	0.078	Polyester	1.159	0.58	✗
12	[106]	Pineapple	1.53	30		3Diso	0.160	Polyester	1.159	0.58	✗
13	[106]	Pineapple	1.53	30		3Diso	0.246	Polyester	1.159	0.58	✗
14	[106]	Pineapple	1.53	30		3Diso	0.336	Polyester	1.159	0.58	✗
15	[106]	Pineapple	1.53	5		3Diso	0.246	Polyester	1.159	0.58	✗
16	[106]	Pineapple	1.53	10		3Diso	0.246	Polyester	1.159	0.58	✗
17	[106]	Pineapple	1.53	20		3Diso	0.246	Polyester	1.159	0.58	✗
18	[106]	Pineapple	1.53	30		3Diso	0.246	Polyester	1.159	0.58	✗
19	[104]	Jute	1.31			3Diso	0.226	PP	0.89		✓
20	[104]	Jute	1.31			3Diso	0.313	PP	0.89		✓
21	[104]	Jute	1.31			3Diso	0.405	PP	0.89		✓
22	[104]	Jute	1.31			3Diso	0.506	PP	0.89		✓
23	[99]	Flax		20	16	3Diso	0.130	PP			✓
24	[99]	Flax		20	16	3Diso	0.200	PP			✓
25	[99]	Flax		20	16	3Diso	0.290	PP			✓
26	[99]	Flax		20	16	3Diso	0.130	PP			✓
27	[99]	Flax		20	16	3Diso	0.200	PP			✓
28	[99]	Flax		20	16	3Diso	0.290	PP			✓
29	[21]	Henequen	1.48	0.49	25	3Diso	0.290	PP	0.91		✓
100	[107]	Hemp	0.86	25	22.5	vMs	0.2	vHDPE	0.95	0.339	✗
101	[107]	Hemp	0.86	25	22.5	vMs	0.3	vHDPE	0.95	0.339	✗
102	[107]	Hemp	0.86	25	22.5	vMs	0.4	vHDPE	0.95	0.339	✗
103	[107]	Hemp	0.86	25	22.5	vMs	0.2	rHDPE	0.95	0.441	✗
104	[107]	Hemp	0.86	25	22.5	vMs	0.3	rHDPE	0.95	0.441	✗
105	[107]	Hemp	0.86	25	22.5	vMs	0.4	rHDPE	0.95	0.441	✗
106	[62]	Flax				vMs	0.100	HDPE		1.2	✓
107	[62]	Flax				vMs	0.180	HDPE		1.2	✓
108	[62]	Flax				vMs	0.200	HDPE		1.2	✓
109	[62]	Flax				vMs	0.300	HDPE		1.2	✓
110	[99]	Flax		20	16	vMs	0.300	Acrylic resin		2.91	✓
111	[99]	Flax		20	16	vMs	0.300	Vinylester		2.99	✓
112	[99]	Flax		20	16	vMs	0.300	Vinylester		3.30	✓
116	[100]	Flax				vMs	0.200	PP	0.91	1.5	✗
117	[100]	Flax				vMs	0.250	PP	0.91	1.5	✗
118	[100]	Flax				vMs	0.300	PP	0.91	1.5	✗
119	[100]	Flax				vMs	0.200	PLA	1.27	3.2	✗
120	[100]	Flax				vMs	0.250	PLA	1.27	3.2	✗
121	[100]	Flax				vMs	0.300	PLA	1.27	3.2	✗
122	[100]	Flax				vMs	0.200	PLLA	1.25	3.32	✓
123	[100]	Flax				vMs	0.250	PLLA	1.25	3.32	✓
124	[100]	Flax				vMs	0.300	PLLA	1.25	3.32	✓

(*continued on next page*)

$$\mathbb{C}_{cw} = \left\{ f_{pn}^{cw}\,\mathbb{C}_{pn} + \frac{f_{celMF}^{cw}}{2\pi}\int_0^{2\pi} \mathbb{C}_{celMF}(\overline{\vartheta},\varphi) : \left[\mathbb{I} + \mathbb{S}_{cyl}^{pn}(\overline{\vartheta},\varphi) : \mathbb{C}_{pn}^{-1} : \left(\mathbb{C}_{celMF}(\overline{\vartheta},\varphi) - \mathbb{C}_{pn}\right)\right]^{-1} \mathrm{d}\varphi \right\} : \left\{ f_{pn}^{cw}\mathbb{I} + \frac{f_{celMF}^{cw}}{2\pi}\int_0^{2\pi} \mathbb{C}_{celMF}(\overline{\vartheta},\varphi) : \left[\mathbb{I} + \mathbb{S}_{cyl}^{pn}(\overline{\vartheta},\varphi) : \mathbb{C}_{pn}^{-1} : \left(\mathbb{C}_{celMF}(\overline{\vartheta},\varphi) - \mathbb{C}_{pn}\right)\right]^{-1} \mathrm{d}\varphi \right\}^{-1} \tag{C.3}$$

with Eshelby tensor components of $\mathbb{S}_{cyl}^{pn}$ given below. The homogenized stiffness of the fiber $\mathbb{C}_{fib}$ follows from the specialization of homogenization rule (12) for $N = 2$ phases, namely cylindrical ($a \to \infty$) and aligned lumen with vanishing stiffness embedded in a cell wall matrix with stiffness according to Eq. (C.3). Mori–Tanaka homogenization ($\mathbb{C}_0 = \mathbb{C}_{cw}$) yields

$$\mathbb{C}_{fib} = f_{cw}^{fib}\,\mathbb{C}_{cw} : \left[f_{cw}^{cel}\mathbb{I} + f_{lum}^{cel}\left(\mathbb{I} - \mathbb{S}_{cyl}^{cw}\right)^{-1}\right]^{-1} \tag{C.4}$$

with Eshelby tensor components of $\mathbb{S}_{cyl}^{cw}$ given below. Finally, the homogenized stiffness of the biocomposite $\mathbb{C}_{comp}$ follows from specialization of homogenization rule (12) for $N = 3$ phases, a polymer matrix phase hosting spherical pores with vanishing stiffness and spheroidal fibers (aspect ratio a) with transversally isotropic stiffness according to Eq. (C.4). For any fiber orientation distribution function f_o, any fiber aspect ratio distribution f_a, and imperfect interfaces according to

Table D.4 (*continued*).

150	[63]	Phormium	1.27			vMF	0.118	Epoxy	1.16	3.91	✓
151	[63]	Phormium	1.27			vMF	0.216	Epoxy	1.16	3.91	✓
152	[63]	Phormium	1.27			vMF	0.315	Epoxy	1.16	3.91	✓
153	[63]	Phormium	1.27			vMF	0.400	Epoxy	1.16	3.91	✓
154	[63]	Phormium	1.27			vMF	0.449	Epoxy	1.16	3.91	✓
155	[63]	Phormium	1.27			vMF	0.499	Epoxy	1.16	3.91	✓
156	[92]	Sisal	1.45	300		vMF	0.516	Epoxy	1.2		✓
157	[92]	Sisal	1.45	300		vMF	0.503	Epoxy	1.2		✓
158	[92]	Sisal	1.45	300		vMF	0.467	Epoxy	1.2		✓
159	[65]	Flax				1D	0.492	PP		1.8	✓
160	[65]	Flax				1D	0.498	PP		1.6	✓
161	[65]	Flax				1D	0.501	Polyamid		1.14	✓
162	[65]	Flax				1D	0.480	Acrylic resin		3.3	✓
163	[65]	Flax				1D	0.509	Epoxy		3.1	✓
164	[93]	Flax		1000	1	1D	0.320	PLA		3.8	✓
165	[93]	Flax		1000	1	1D	0.320	PHA		4.4	✓
166	[93]	Flax		1000	1	1D	0.320	PBS		0.75	✓
167	[93]	Flax		1000	1	1D	0.320	PP		1.58	✓
168	[93]	Flax		1000	1	1D	0.320	PP		1.4	✓
169	[94]	Flax				1D	0.210	Epoxy	1.15	3.15	✓
170	[94]	Flax				1D	0.420	Epoxy	1.15	3.15	✓
171	[94]	Flax				1D	0.470	Epoxy	1.15	3.15	✓
172	[94]	Flax				1D	0.320	Epoxy	1.15	3.15	✓
173	[95]	Sisal				1D	0.280	Epoxy	1.15	3.15	✓
174	[95]	Sisal				1D	0.350	Epoxy	1.15	3.15	✓
175	[95]	Sisal				1D	0.460	Epoxy	1.15	3.15	✓
176	[96]	Alfa	1.4	350	44	1D	0.450	Polyester	1.2	4	✓
177	[96]	Alfa	1.4	350	44	1D	0.450	Polyester	1.2	4	✓
178	[96]	Alfa	1.4	350	44	1D	0.450	Polyester	1.2	4	✓
179	[96]	Alfa	1.4	350	44	1D	0.450	Polyester	1.2	4	✓
180	[96]	Alfa	1.4	350	44	1D	0.450	Polyester	1.2	4	✓
181	[97]	Kenaf		35	46.8	vMF	0.404	PLA	1.24	2.1	✓
182	[97]	Kenaf		35	46.8	vMF	0.406	PHB	1.25	3.5	✓
183	[98]	Kenaf		500	100	vMF	0.300	PLA	1.2	3.8	✓
184	[98]	Kenaf		500	100	vMF	0.500	PLA	1.2	3.8	✓
185	[98]	Kenaf		500	100	vMF	0.700	PLA	1.2	3.8	✓
186	[108]	Jute		200		vMF	0.09	Polyester	1.2	1.36	✗
187	[108]	Jute		200		vMF	0.18	Polyester	1.2	1.36	✗
188	[108]	Jute		200		vMF	0.28	Polyester	1.2	1.36	✗
189	[108]	Jute		200		vMF	0.37	Polyester	1.2	1.36	✗
190	[108]	Jute		200		vMF	0.47	Polyester	1.2	1.36	✗

ad #3: aspect ratio distribution measured from Bourmaud et al. [22], lognormal distribution fitted with parameters according to Fig. A.9.
ad #10: Experimentally measured modulus does not increase, despite more fibers, possible air volume.
ad #19–22,29: compatilizer used, experimentally tested moduli in Fig. 3 refer to plateau values indicating perfect bond.
ad #29: chemical fiber characterization performed, mass fractions amount to 0.681 for total cellulose, 0.182 for hemicellulose, 0.087 for lignin, translation to volume fractions according to Königsberger et al. [19].
ad #116–124: some debonding is observed.
ad #150–155: air volume quantified, amounts to $f_{mpor}^{comp} \in \{0, 0.014, 0.024, 0.049, 0.043, 0.062\}$, respectively, for the six mixes; lumen porosity measured $f_{lum}^{fib} = 0.214$.
ad #156–158: lumen porosity measured $f_{lum}^{fib} \in \{0.27, 0.23, 0.096\}$, respectively, for the three mixes.
ad #159–168,172: Flax tape is used. Thus, the fibers are perfectly parallel and their aspect ratio $a \to \infty$.
ad #169–171,173–180: Fiber mats or clothes are used, thus the fibers are perfectly parallel.
ad #176–180: loading direction with respect to fiber orientation is changed, it amounts to 0° for #176, 10° for #177, 30° for #178, 45° for #179, 90° for #180.
ad #176–180: air volume quantified, amounts to $f_{mpor}^{comp} \in \{0.136, 0.067\}$, respectively, for the two mixes.

Eqs. (1) and (2), Mori–Tanaka homogenization ($\mathbb{C}_0 = C_{pm}$) yields

$$\begin{aligned}\mathbb{C}_{comp} = \Bigg\{ & f_{pm}^{comp}\,\mathbb{C}_{pm} + f_{fib}^{comp} \int_0^{2\pi}\int_0^{\pi} f_o(\vartheta,\varphi)\,\mathbb{C}_{fib}(\vartheta,\varphi) \\ & : \mathbb{A}_{allfib,0}(\vartheta,\varphi)\sin\vartheta\,\mathrm{d}\vartheta\,\mathrm{d}\varphi \Bigg\}^{-1} : \\ & \Bigg\{ f_{pm}^{comp}\,\mathbb{I} + f_{mpor}^{comp}\left(\mathbb{I} - \mathbb{S}_{sph}^{pm}\right)^{-1} + f_{fib}^{comp}\int_0^{2\pi}\int_0^{\pi} f_o(\vartheta,\varphi) \\ & \times\ \mathbb{A}_{allfib,0}(\vartheta,\varphi)\sin\vartheta\,\mathrm{d}\vartheta\,\mathrm{d}\varphi \Bigg\}^{-1}\end{aligned} \tag{C.5}$$

with auxiliary tensor $\tilde{\mathbb{A}}_{allfib,0}$ reading as

$$\begin{aligned}\mathbb{A}_{allfib,0}(\vartheta,\varphi) = \int_0^{\infty} f_a(a) \Big\{ & \left[\mathbb{I} + \mathbb{S}_{fib}^{pm}(\vartheta,\varphi;a) : \mathbb{C}_{pm}^{-1} : \left(\mathbb{C}_{fib}(\vartheta,\varphi) - \mathbb{C}_{pm}\right)\right]^{-1} + \\ & \left[\mathbb{I} - \mathbb{S}_i(\vartheta,\varphi;a)\right] : \mathbb{R}_{fib/pm}(\vartheta,\varphi;a) : \mathbb{C}_{fib}(\vartheta,\varphi)\,\mathrm{d}a \Big\}^{-1}.\end{aligned} \tag{C.6}$$

If orientation distributions are not uniform, $\mathbb{C}_{comp}$ is symmetrized [115].

To complete the analytical formula set, Eshelby tensor expressions are required. We deal with Eshelby problems involving spheroidal inclusions i in matrices with stiffness tensor $\mathbb{C}_m$. As for spherical inclusions embedded in a polymer network matrix, the Eshelby tensor components read as [18]

$$\begin{aligned}S_{\mathrm{sph},ijkl}^{\mathrm{pm}} = & \frac{5\nu_{\mathrm{pm}} - 1}{15\left(1 - \nu_{\mathrm{pm}}\right)}\delta_{ij}\,\delta_{kl} + \\ & \frac{4 - 5\nu_{\mathrm{pm}}}{15\left(1 - \nu_{\mathrm{pm}}\right)}\left(\delta_{ik}\,\delta_{jl} + \delta_{il}\,\delta_{jk}\right),\end{aligned} \tag{C.7}$$

with δ_{ij} denoting the Kronecker delta. As for the cylindrical cellulose inclusions (nanofibrils and microfibrils, respectively), the infinite matrix in the corresponding Eshelby problem is isotropic, such that non-zero components with respect to the local orthonormal coordinate

Table E.5
Model-predicted stiffness constants for transversally isotropic plant fibers; average values referring to average cell wall volume fractions and average microfibrill angles.

	E_T [GPa]	E_L [GPa]	ν_T [–]	ν_{LT} [–]	μ_{LT} [GPa]
Banana	7.39	48.69	0.37	0.28	6.72
Flax	8.27	84.84	0.31	0.16	6.63
Hemp	9.30	79.19	0.32	0.18	7.25
Isora	6.61	50.52	0.25	0.61	16.17
Jute	7.22	59.96	0.33	0.22	6.25
Kenaf	6.04	46.79	0.34	0.27	6.27
Ramie	9.19	79.41	0.33	0.21	7.76
Sorghum	3.34	25.09	0.34	0.32	4.00
Alfa	3.36	24.12	0.34	0.27	3.28
Bagasse	0.93	21.23	0.28	0.65	2.49
Bamboo	2.97	28.69	0.31	0.24	2.64
Abaca	7.79	38.69	0.29	0.49	12.68
Curaua	4.64	64.55	0.26	0.64	13.68
Henequen	7.48	37.82	0.33	0.41	10.12
Phormium	8.31	58.04	0.34	0.23	7.03
Pineapple	10.33	58.29	0.37	0.28	8.92
Sisal	6.26	51.88	0.29	0.50	12.63
Coir	5.39	7.68	0.24	0.38	7.11
Kapok	0.94	10.75	0.33	0.27	1.04
Oil Palm	6.35	7.36	0.19	0.41	8.81
Barley	0.92	11.38	0.33	0.27	1.12
Cornhusk	1.94	22.54	0.33	0.22	2.02
Cornstalk	0.44	15.89	0.32	0.38	0.94
Rice	6.73	32.04	0.32	0.25	5.71
Soybean	1.62	21.14	0.34	0.28	1.89
Wheat	3.39	28.51	0.32	0.21	2.58

base x_1, x_2, x_3 (with x_3 as the cylinder axis direction) read as [116]

$$\begin{aligned} S^m_{\text{cyl},2222} &= S^m_{\text{cyl},3333} = \frac{5-4\nu_m}{8\,(1-\nu_m)} \\ S^m_{\text{cyl},2233} &= S^m_{\text{cyl},3322} = \frac{-1+4\nu_m}{8\,(1-\nu_m)} \\ S^m_{\text{cyl},1313} &= S^m_{\text{cyl},1212} = \frac{1}{4} \\ S^m_{\text{cyl},2323} &= \frac{3-4\nu_m}{8\,(1-\nu_m)}\,, \end{aligned} \tag{C.8}$$

where m stands either for the amorphous cellulose matrix (for nanofibril inclusions), or for the polymer network matrix (for microfibril inclusions). As for the cylindrical lumen pores, the infinite matrix in the corresponding Eshelby problem is transversally isotropic, and the cylinder axis is aligned with the matrix's axis of transverse symmetry. This way, the Eshelby tensor reads as [117]

$$\begin{aligned} \mathbb{S}^{\text{cw}}_{\text{cyl}} = &\frac{C_{\text{cw},1}}{2C_{\text{cw},1}+C_{\text{cw},2}}\mathbb{T}^{(1)} + \frac{C_{\text{cw},1}+C_{\text{cw},2}}{2C_{\text{cw},1}+C_{\text{cw},2}}\mathbb{T}^{(2)} + \\ &\frac{C_{\text{cw},3}}{2C_{\text{cw},1}+C_{\text{cw},2}}\mathbb{T}^{(3)} + \mathbb{T}^{(5)}\,. \end{aligned} \tag{C.9}$$

With x_3 as the axis of transverse symmetry, tensors $T^{(1)}, \dots, T^{(5)}$ have the following non-zero components

$$\begin{aligned} &T^{(1)}_{1111} = T^{(1)}_{2222} = T^{(1)}_{1122} = T^{(1)}_{2211} = 1 \\ &T^{(2)}_{1212} = T^{(2)}_{2121} = T^{(2)}_{1221} = T^{(2)}_{2112} = T^{(2)}_{1111} = T^{(2)}_{2222} = \\ &\quad -T^{(2)}_{1122} = -T^{(2)}_{2211} = \frac{1}{2} \\ &T^{(3)}_{1133} = T^{(3)}_{2233} = 1 \\ &T^{(5)}_{1313} = T^{(5)}_{2323} = T^{(5)}_{1331} = T^{(5)}_{2332} = T^{(5)}_{3113} = T^{(5)}_{3223} = \\ &\quad T^{(5)}_{3131} = T^{(5)}_{3132} = \frac{1}{4}\,. \end{aligned} \tag{C.10}$$

and $C_{\text{cw},1}$, $C_{\text{cw},2}$, and $C_{\text{cw},3}$ read as

$$\begin{aligned} C_{\text{cw},1} &= \left(C_{\text{cw},1111} + C_{\text{cw},1122}\right)/2\,, \\ C_{\text{cw},2} &= 2\,C_{\text{cw},1212}\,, \\ C_{\text{cw},3} &= C_{\text{cw},1133}\,, \end{aligned} \tag{C.11}$$

As for general spheroidal inclusion in an anisotropic matrix, as required for the homogenization of the composite scale containing technical fibers, expressions for the Eshelby tensor are obtained after integration of Green's functions, see Mura [116] for details.

Compliant interfaces are considered only between fibers (with aspect ratio $a > 1$) and matrix at the composite scale. The corresponding interface tensor $R_{fib/pm}$ for prolate fibers with diameter d_f aligned with the global x_3-axis can be obtained after integration of Eq. (5) as [118]

$$\mathbb{R}_{fib/pm} = \alpha\mathbb{P} + (\beta-\alpha)\mathbb{Q}\,, \tag{C.12}$$

with α and β as interface compliance defined in (2) and with auxiliary tensors $\mathbb{P}$ and $\mathbb{Q}$ whose non-zero (independent) components read as

$$\begin{aligned} P_{1111} &= \frac{3}{4d_f}\left[\frac{a}{\sqrt{a^2-1}}\frac{a^2-2}{2(a^2-1)}\arcsin\left(\frac{\sqrt{a^2-1}}{a}\right) + \frac{a}{2(a^2-1)}\right] \\ P_{3333} &= \frac{3}{2d_f}\left[\frac{a}{(a^2-1)^{3/2}}\arcsin\left(\frac{\sqrt{a^2-1}}{a}\right) - \frac{1}{a(a^2-1)}\right] \\ P_{1313} &= \frac{1}{4}(P_{1111}+P_{3333}) \\ P_{1212} &= \frac{1}{2}P_{1111} \end{aligned} \tag{C.13}$$

$$\begin{aligned} Q_{1111} &= \frac{3}{2d_f}\left[\frac{a(2+a^2)}{(a^2-1)^2} + \frac{a^3(a^2-4)}{(a^2-1)^{5/2}}\arcsin\left(\frac{\sqrt{a^2-1}}{a}\right)\right] \\ Q_{3333} &= \frac{3}{2d_f}\left[\frac{2a^2+1}{a(a^2-1)^2} - \frac{3a}{(a^2-1)^{5/2}}\arcsin\left(\frac{\sqrt{a^2-1}}{a}\right)\right] \\ Q_{1133} &= \frac{3}{4d_f}\left[\frac{a(a^2+2)}{(a^2-1)^{5/2}}\arcsin\left(\frac{\sqrt{a^2-1}}{a}\right) - \frac{3a}{(a^2-1)^2}\right] \\ Q_{1122} &= \frac{1}{3}Q_{1111} \end{aligned} \tag{C.14}$$

Appendix D. Model input for validation

Here, we list the model input data for the 73 composite materials studied for model validation.

Appendix E. Fiber stiffness

The model-predicted fiber stiffness tensor components based on average cell wall volume fraction (Table 2) and average microfibril angles (Table 3) is summarized. The transversally orthotropic fiber stiffness tensor $\mathbb{C}_{fib}$ is therefore expressed as a transversally orthotropic tensor with compliance $\mathbb{C}^{-1}_{fib}$ expressed in the fiber-specific R-T-L base frame (where the isotropic plane is the R-T-plane) as

$$\mathbb{C}^{-1}_{fib} = \begin{bmatrix} 1/E_T & -\nu_T/E_T & -\nu_{LT}/E_L & 0 & 0 & 0 \\ & 1/E_T & -\nu_{TL}/E_L & 0 & 0 & 0 \\ & & 1/E_L & 0 & 0 & 0 \\ \vdots & & & 1/\mu_{LT} & 0 & 0 \\ & \iddots & & & 1/\mu_{LT} & 0 \\ \text{sym} & & \dots & & & 2(1+\nu_T)/E_T \end{bmatrix}_{\mathfrak{e}_R\text{-}\mathfrak{e}_T\text{-}\mathfrak{e}_L}. \tag{E.1}$$

with E_T and ν_T as modulus and Poisson's ratio in the symmetry plane, E_L and as moduli and ν_{LT} as out-of-plane counterparts and μ_{LT} as corresponding shear modulus. Note that (E.1) refers to Mandel notation. The five elastic constants are listed for all 26 different plants in Table E.5.

References

[1] Bledzki AK, Gassan J. Composites reinforced with cellulose based fibres. Prog Polym Sci 1999;24:221–74. http://dx.doi.org/10.1016/S0079-6700(98)00018-5.

[2] Dicker Michael PM, Duckworth Peter F, Baker Anna B, Francois Guillaume, Hazzard Mark K, Weaver Paul M. Green composites: A review of material attributes and complementary applications. Composites A 2014;56:280–9. http://dx.doi.org/10.1016/j.compositesa.2013.10.014.

[3] Pickering KL, Efendy M GAruan, Le TM. A review of recent developments in natural fibre composites and their mechanical performance. Composites A 2016;83:98–112. http://dx.doi.org/10.1016/j.compositesa.2015.08.038.

[4] tak Lau Kin, yan Hung Pui, Zhu Min Hao, Hui David. Properties of natural fibre composites for structural engineering applications. Composites B 2018;136:222–33. http://dx.doi.org/10.1016/j.compositesb.2017.10.038.

[5] Fidelis Maria Ernestina Alves, Pereira Thatiana Vitorino Castro, Gomes Otávio Da Fonseca Martins, Silva Flávio De Andrade, Filho Romildo Dias Toledo. The effect of fiber morphology on the tensile strength of natural fibers. J Mater Res Technol 2013;2:149–57. http://dx.doi.org/10.1016/j.jmrt.2013.02.003.

[6] Shinoj S, Visvanathan R, Panigrahi S, Kochubabu M. Oil palm fiber (OPF) and its composites: A review. Ind Crops Prod 2011;33:7–22. http://dx.doi.org/10.1016/j.indcrop.2010.09.009.

[7] Sathishkumar TP, Navaneethakrishnan P, Shankar S, Rajasekar R, Rajini N. Characterization of natural fiber and composites - A review. J Reinf Plast Compos 2013;32:1457–76. http://dx.doi.org/10.1177/0731684413495322.

[8] Feng Yuqi, Hao Huali, Lu Haibao, Chow Cheuk Lun, Lau Denvid. Exploring the development and applications of sustainable natural fiber composites: A review from a nanoscale perspective. Composites B 2024;276:111369. http://dx.doi.org/10.1016/j.compositesb.2024.111369.

[9] Huang Zheng-Ming. Chapter One - Mechanics theories for anisotropic or composite materials. In: Bordas Stéphane PA, editor. In: Advances in applied mechanics, vol. 56, Elsevier; 2023, p. 1–137. http://dx.doi.org/10.1016/bs.aams.2022.09.004.

[10] Munde Yashwant S, Ingle Ravindra B. Theoretical modeling and experimental verification of mechanical properties of natural fiber reinforced thermoplastics. Proc Technol 2015;19:320–6. http://dx.doi.org/10.1016/j.protcy.2015.02.046.

[11] Delgado-Aguilar M, Julián F, Tarrés Q, Méndez JA, Mutjé P, Espinach FX. Bio composite from bleached pine fibers reinforced polylactic acid as a replacement of glass fiber reinforced polypropylene, macro and micro-mechanics of the Young's modulus. Composites B 2017;125:203–10. http://dx.doi.org/10.1016/j.compositesb.2017.05.058.

[12] Zuccarello B, Scaffaro R. Experimental analysis and micromechanical models of high performance renewable agave reinforced biocomposites. Composites B 2017;119:141–52. http://dx.doi.org/10.1016/j.compositesb.2017.03.056.

[13] Alhijazi Mohamad, Zeeshan Qasim, Qin Zhaoye, Safaei Babak, Asmael Mohammed. Finite element analysis of natural fibers composites: A review. Nanotechnol Rev 2020;9:853–75. http://dx.doi.org/10.1515/ntrev-2020-0069.

[14] Hirsch Teddy J. Modulus of elasticity iof concrete affected by elastic moduli of cement paste matrix and aggregate. ACI J Proc 1962;59:427–52. http://dx.doi.org/10.14359/7924.

[15] Cox HL. The elasticity and strength of paper and other fibrous materials. Br J Appl Phys 1952;3:72–9. http://dx.doi.org/10.1088/0508-3443/3/3/302.

[16] Krenchel Herbert. Fibre reinforcement; theoretical and practical investigations of the elasticity and strength of fibre-reinforced materials. Akademisk forlag; 1964.

[17] Halpin JC. Stiffness and expansion estimates for oriented short fiber composites. J Compos Mater 1969;3:732–4. http://dx.doi.org/10.1177/002199836900300419.

[18] Zaoui A. Continuum micromechanics: Survey. J Eng Mech 2002;128:808–16.

[19] Königsberger Markus, Lukacevic Markus, Füssl Josef. Multiscale micromechanics modeling of plant fibers: upscaling of stiffness and elastic limits from cellulose nanofibrils to technical fibers. Mater Struct/Mater Constr 2023;56. http://dx.doi.org/10.1617/s11527-022-02097-2.

[20] Duigou Antoine Le, Baley Christophe, Grohens Yves, Davies Peter, Cognard Jean Yves, Créach'Cadec Romain, Sohier Laurent. A multi-scale study of the interface between natural fibres and a biopolymer. Composites A 2014;65:161–8. http://dx.doi.org/10.1016/j.compositesa.2014.06.010.

[21] Tarrés Quim, Vilaseca Fabiola, Herrera-Franco Pedro J, Espinach F Xavier, Delgado-Aguilar Marc, Mutjé Pere. Interface and micromechanical characterization of tensile strength of bio-based composites from polypropylene and henequen strands. Ind Crops Prod 2019;132:319–26. http://dx.doi.org/10.1016/j.indcrop.2019.02.010.

[22] Bourmaud A, Ausias G, Lebrun G, Tachon ML, Baley C. Observation of the structure of a composite polypropylene/flax and damage mechanisms under stress. Ind Crops Prod 2013;43:225–36. http://dx.doi.org/10.1016/j.indcrop.2012.07.030.

[23] Moigne Nicolas Le, Oever Martien Van Den, Budtova Tatiana. A statistical analysis of fibre size and shape distribution after compounding in composites reinforced by natural fibres. Composites A 2011;42:1542–50. http://dx.doi.org/10.1016/j.compositesa.2011.07.012.

[24] Madsen Bo, Thygesen Anders, Lilholt Hans. Plant fibre composites - porosity and volumetric interaction. Compos Sci Technol 2007;67:1584–600. http://dx.doi.org/10.1016/j.compscitech.2006.07.009.

[25] Madsen Bo, Thygesen Anders, Lilholt Hans. Plant fibre composites - porosity and stiffness. 2009, http://dx.doi.org/10.1016/j.compscitech.2009.01.016.

[26] Qu Jianmin. Eshelby tensor for an elastic inclusion with slightly weakened interface. J Appl Mech Trans ASME 1993;60:1048–50. http://dx.doi.org/10.1115/1.2900974.

[27] Hashin Z. The spherical inclusion with imperfect interface. J Appl Mech 1991;58:444.

[28] Mirkhalaf SM, Eggels EH, van Beurden T JH, Larsson F, Fagerström M. A finite element based orientation averaging method for predicting elastic properties of short fiber reinforced composites. Composites B 2020;202:108388. http://dx.doi.org/10.1016/j.compositesb.2020.108388.

[29] Volk Maximilian, Yuksel Onur, Baran Ismet, Hattel Jesper H, Spangenberg Jon, Sandberg Michael. Cost-efficient, automated, and sustainable composite profile manufacture: A review of the state of the art, innovations, and future of pultrusion technologies. Composites B 2022;246:110135. http://dx.doi.org/10.1016/j.compositesb.2022.110135.

[30] Ren Lei, Wang Zhenguo, Ren Luquan, Xu Chao, Li Bingqian, Shi Yusheng, Liu Qingping. Understanding the role of process parameters in 4D printing: A review. Composites B 2023;265:110938. http://dx.doi.org/10.1016/j.compositesb.2023.110938.

[31] Gager Victor, Legland David, Bourmaud Alain, Le Duigou Antoine, Pierre Floran, Behlouli Karim, Baley Christophe. Oriented granulometry to quantify fibre orientation distributions in synthetic and plant fibre composite preforms. Ind Crops Prod 2020;152:112548. http://dx.doi.org/10.1016/j.indcrop.2020.112548.

[32] Šeta Berin, Sandberg Michael, Brander Marco, Mollah Md Tusher, Pokkalla Deepak, Kumar Vipin, Spangenberg Jon. Modeling fiber orientation and strand shape morphology in three-dimensional material extrusion additive manufacturing. Composites B 2023;266:110957. http://dx.doi.org/10.1016/j.compositesb.2023.110957.

[33] Hofstetter Karin, Hellmich Christian, Eberhardsteiner Josef. Development and experimental validation of a continuum micromechanics model for the elasticity of wood. Eur J Mech A Solids 2005;24:1030–53. http://dx.doi.org/10.1016/j.euromechsol.2005.05.006.

[34] Bader TK, Hofstetter K, Hellmich C, Eberhardsteiner J. The poroelastic role of water in cell walls of the hierarchical composite "softwood". Acta Mech 2011;217:75–100.

[35] Gangwar Tarun, Schillinger Dominik. Microimaging-informed continuum micromechanics accurately predicts macroscopic stiffness and strength properties of hierarchical plant culm materials. Mech Mater 2019;130:39–57. http://dx.doi.org/10.1016/j.mechmat.2019.01.009.

[36] Eshelby JD. The determination of the elastic field of an ellipsoidal inclusion, and related problems. Proc R Soc Lond Ser A 1957;241:376–96.

[37] Qu Jianmin. The effect of slightly weakened interfaces on the overall elastic properties of composite materials. Mech Mater 1993;14:269–81. http://dx.doi.org/10.1016/0167-6636(93)90082-3.

[38] Mori T, Tanaka K. Average stress in matrix and average elastic energy of materials with misfitting inclusions. Acta Metall 1973;21:571–4. http://dx.doi.org/10.1016/0001-6160(73)90064-3.

[39] Benveniste Y. A new approach to the application of mori-tanaka's theory in composite materials. Mech Mater 1987;6:147–57. http://dx.doi.org/10.1016/0167-6636(87)90005-6.

[40] Hershey AV, A. Dahlgren V. The elasticity of an isotropic aggregate of anisotropic cubic crystals. J Appl Mech Trans 1954;21:236–40. http://dx.doi.org/10.1002/prca.201200064.

[41] Hill R. A self-consistent mechanics of composite materials. J Mech Phys Solids 1965;13:213–22.

[42] Hashin Z. Thermoelastic properties of particulate composites with imperfect interface. J Mech Phys Solids 1991;39:745–62.

[43] Yanase K, Ju JW. Effective elastic moduli of spherical particle reinforced composites containing imperfect interfaces. Int J Damage Mech 2012;21:97–127. http://dx.doi.org/10.1177/1056789510397076.

[44] Dinzart F, Sabar H. New micromechanical modeling of the elastic behavior of composite materials with ellipsoidal reinforcements and imperfect interfaces. Int J Solids Struct 2017;108:254–62. http://dx.doi.org/10.1016/j.ijsolstr.2016.12.024.

[45] Dinzart F, Sabar H. Unpupblished appendix to: New micromechanical modeling of the elastic behavior of composite materials with ellipsoidal reinforcements and imperfect interfaces. 2017.

[46] Königsberger Markus, Pichler Bernhard, Hellmich Christian. Multiscale poroelasticity of densifying calcium-silicate hydrates in cement paste: An experimentally validated continuum micromechanics approach. Internat J Engrg Sci 2020;147. http://dx.doi.org/10.1016/j.ijengsci.2019.103196.

[47] Tashiro Kohji, Kobayashi Masamichi. Calculation of crystallite modulus of native cellulose. Polym Bull 1985;14:213–8. http://dx.doi.org/10.1007/BF00254940.

[48] Schwaighofer Michael, Zelaya-Lainez Luis, Königsberger Markus, Lukacevic Markus, Serna-Loaiza Sebastián, Harasek Michael, Lahayne Olaf, Senk Valentin, Füssl Josef. Characterization of mechanical properties of five hot-pressed lignins extracted from different feedstocks by microscopy-aided nanoindentation. Mater Des 2023;227:111765. http://dx.doi.org/10.1016/j.matdes.2023.111765.

[49] Schwaighofer Michael, Königsberger Markus, Zelaya-Lainez Luis, Lukacevic Markus, Serna-Loaiza Sebastián, Harasek Michael, Zikeli Florian, Friedl Anton, Füssl Josef. The viscoelastic behavior of lignin: Quantification through nanoindentation relaxation testing on hot-pressed technical lignin samples from various origins. Mech Mater 2024;188:104864. http://dx.doi.org/10.1016/j.mechmat.2023.104864.

[50] Kulasinski Karol, Keten Sinan, Churakov Sergey V, Derome Dominique, Carmeliet Jan. A comparative molecular dynamics study of crystalline, paracrystalline and amorphous states of cellulose. Cellulose 2014;21:1103–16. http://dx.doi.org/10.1007/s10570-014-0213-7.

[51] O'Sullvian ACC. Cellulose: the structure slowly unravels. Cellulose 1997;4:173–207. http://dx.doi.org/10.1023/A:1018431705579.

[52] Chen Hongzhang. Biotechnology of lignocellulose. Dordrecht, Netherlands: Springer Netherlands; 2014, http://dx.doi.org/10.1007/978-94-007-6898-7.

[53] Youssefian S, Jakes JE, Rahbar N. Variation of nanostructures, molecular interactions, and anisotropic elastic moduli of lignocellulosic cell walls with moisture. Sci Rep 2017;7:2054. http://dx.doi.org/10.1038/s41598-017-02288-w.

[54] Cousins WJ. Young's modulus of hemicellulose as related to moisture content. Wood Sci. Technol. 1978;12:161–7. http://dx.doi.org/10.1007/BF00372862.

[55] Cousins WJ. Elastic modulus of lignin as related to moisture content. Wood Sci. Technol. 1976;10:9–17.

[56] Salbu Linda. Compressibility and compactibility of pectin powders -a study of their potential as direct compression excipients in tablets (Ph.D. thesis), University of Tromsø; 2011.

[57] Pabst Willi, Gregorová Eva. Elastic properties of silica polymorphs-a review. Ceramics - Silikaty 2013;57:167–84.

[58] Bledzki AK, Mamun AA, Lucka-Gabor M, Gutowski VS. The effects of acetylation on properties of flax fibre and its polypropylene composites. Express Polym Lett 2008;2:413–22. http://dx.doi.org/10.3144/expresspolymlett.2008.50.

[59] CROW. Chemical retrieval on the web, polymer database. 2022, URL https://polymerdatabase.com/.

[60] Du Yicheng, Wu Tongfei, Yan Ning, Kortschot Mark T, Farnood Ramin. Fabrication and characterization of fully biodegradable natural fiber-reinforced poly(lactic acid) composites. Composites B 2014;56:717–23. http://dx.doi.org/10.1016/j.compositesb.2013.09.012.

[61] Ferreira Rafael Thiago Luiz, Amatte Igor Cardoso, Dutra Thiago Assis, Bürger Daniel. Experimental characterization and micrography of 3D printed PLA and PLA reinforced with short carbon fibers. Composites B 2017;124:88–100. http://dx.doi.org/10.1016/j.compositesb.2017.05.013.

[62] Singleton A CN, Baillie CA, Beaumont P WR, Peijs T. On the mechanical properties, deformation and fracture of a natural fibre/recycled polymer composite. Composites B 2003;34:519–26. http://dx.doi.org/10.1016/S1359-8368(03)00042-8.

[63] Le Tan Minh, Pickering Kim Louise. The potential of harakeke fibre as reinforcement in polymer matrix composites including modelling of long harakeke fibre composite strength. Composites A 2015;76:44–53. http://dx.doi.org/10.1016/j.compositesa.2015.05.005.

[64] Saseendran Sibin, Wysocki Maciej, Varna Janis. Cure-state dependent viscoelastic Poisson's ratio of LY5052 epoxy resin. Adv Manuf: Polym Compos Sci 2017;3:92–100. http://dx.doi.org/10.1080/20550340.2017.1348002.

[65] Baley Christophe, Lan Marine, Bourmaud Alain, Duigou Antoine Le. Compressive and tensile behaviour of unidirectional composites reinforced by natural fibres: Influence of fibres (flax and jute), matrix and fibre volume fraction. Mater Today Commun 2018;16:300–6. http://dx.doi.org/10.1016/j.mtcomm.2018.07.003.

[66] Mwaikambo L. Review of the history, properties and application of plant fibres. Afr J Sci Technol 2006;7:121.

[67] Petroudy SR Djafari. Physical and mechanical properties of natural fibers. In: Advanced high strength natural fibre composites in construction. Elsevier; 2017, p. 59–83. http://dx.doi.org/10.1016/B978-0-08-100411-1.00003-0.

[68] Reddy Narendra, Yang Yiqi. Biofibers from agricultural byproducts for industrial applications. Trends Biotechnol 2005;23:22–7. http://dx.doi.org/10.1016/j.tibtech.2004.11.002.

[69] Rowell RM. Natural fibres: Types and properties. In: Properties and performance of natural-fibre composites. 2008, p. 3–66. http://dx.doi.org/10.1533/9781845694593.1.3.

[70] André Alann. Fibres for strengthening of timber structures. 2006.

[71] Zimniewska Malgorzata, Wladyka-Przybylak Maria, Mankowski Jerzy. Cellulosic bast fibers, their structure and properties suitable for composite applications. In: Kalia Susheel, Kaith BS, Kaur Inderjeet, editors. Cellulose fibers: bio- and nano-polymer composites. Berlin, Heidelberg: Springer Berlin Heidelberg; 2011, p. 97–119. http://dx.doi.org/10.1007/978-3-642-17370-7.

[72] Reddy Narendra, Yang Yiqi. Preparation and characterization of long natural cellulose fibers from wheat straw. J Agricult Food Chem 2007;55:8570–5. http://dx.doi.org/10.1021/jf071470g.

[73] Reddy Narendra, Yang Yiqi. Structure and properties of natural cellulose fibers obtained from sorghum leaves and stems. J Agricult Food Chem 2007;55:5569–74. http://dx.doi.org/10.1021/jf0707379.

[74] Ashori Alireza, Nourbakhsh Amir, Tabrizi Ali Kazemi. Thermoplastic hybrid composites using bagasse, corn stalk and E-glass fibers: Fabrication and characterization. Polym Plast Technol Eng 2014;53:1–8. http://dx.doi.org/10.1080/03602559.2013.832854.

[75] Sfiligoj M, Hribernik S, Stana K, Kree T. Plant fibres for textile and technical applications. Adv Agrophys Res 2013. http://dx.doi.org/10.5772/52372.

[76] Rusch Fernando, Ceolin Guilherme Bordignon, Hillig Éverton. Morphology, density and dimensions of bamboo fibers: A bibliographical compilation. Pesquisa Agropecuaria Trop 2019;49. http://dx.doi.org/10.1590/1983-40632019v4955007.

[77] Tomczak Fábio, Satyanarayana Kestur Gundappa, Sydenstricker Thais Helena Demétrio. Studies on lignocellulosic fibers of Brazil: Part III - morphology and properties of Brazilian curauá fibers. Composites A 2007;38:2227–36. http://dx.doi.org/10.1016/j.compositesa.2007.06.005.

[78] Reddy Narendra, Yang Yiqi. Structure and properties of high quality natural cellulose fibers from cornstalks. Polymer 2005;46:5494–500. http://dx.doi.org/10.1016/j.polymer.2005.04.073.

[79] Martelli-Tosi Milena, Assis Odílio BG, Silva Natália C, Esposto Bruno S, Martins Maria Alice, Tapia-Blácido Delia R. Chemical treatment and characterization of soybean straw and soybean protein isolate/straw composite films. Carbohydr Polymers 2017;157:512–20. http://dx.doi.org/10.1016/j.carbpol.2016.10.013.

[80] Yu Hui, Liu Ruigang, Shen Dawa, Wu Zhonghua, Huang Yong. Arrangement of cellulose microfibrils in the wheat straw cell wall. Carbohydr Polymers 2008;72:122–7. http://dx.doi.org/10.1016/j.carbpol.2007.07.035.

[81] Faruk Omar, Bledzki Andrzej K, Fink Hans-Peter, Sain Mohini. Biocomposites reinforced with natural fibers: 2000–2010. Prog Polym Sci 2012;37:1552–96. http://dx.doi.org/10.1016/j.progpolymsci.2012.04.003.

[82] Summerscales John, Dissanayake Nilmini PJ, Virk Amandeep S, Hall Wayne. A review of bast fibres and their composites. Part 1 – fibres as reinforcements. Composites A 2010;41:1329–35. http://dx.doi.org/10.1016/j.compositesa.2010.06.001.

[83] Suryanto Hero, Marsyahyo Eko, Irawan Yudy Surya, Soenoko Rudy. Morphology, structure, and mechanical properties of natural cellulose fiber from mendong grass (fimbristylis globulosa). J Natural Fibers 2014;11:333–51. http://dx.doi.org/10.1080/15440478.2013.879087.

[84] Ramesh M, Palanikumar K, Reddy K Hemachandra. Plant fibre based biocomposites: Sustainable and renewable green materials. Renew Sustain Energy Rev 2017;79:558–84. http://dx.doi.org/10.1016/j.rser.2017.05.094.

[85] Hu Wei, Ton-That Minh-Tan, Perrin-Sarazin Florence, Denault Johanne. An improved method for single fiber tensile test of natural fibers. Polym Eng Sci 2010;50:819–25. http://dx.doi.org/10.1002/pen.21593.

[86] Silva Flavio de Andrade, Chawla Nikhilesh, de Toledo Filho Romildo Dias. Tensile behavior of high performance natural (sisal) fibers. Compos Sci Technol 2008;68:3438–43. http://dx.doi.org/10.1016/j.compscitech.2008.10.001.

[87] Andersons Janis, Sparniņš E, Joffe R, Wallström L. Strength distribution of elementary flax fibres. Compos Sci Technol 2005;65:693–702. http://dx.doi.org/10.1016/j.compscitech.2004.10.001.

[88] Symington Mark C, Banks W M, West Opukuro David, Pethrick R A. Tensile testing of cellulose based natural fibers for structural composite applications MAR. J Compos Mater 2009. http://dx.doi.org/10.1177/0021998308097740.

[89] Zuccarello Bernardo, Militello Carmelo, Bongiorno Francesco. Influence of the anisotropy of sisal fibers on the mechanical properties of high performance unidirectional biocomposite lamina and micromechanical models. Composites A 2021;143:106320. http://dx.doi.org/10.1016/j.compositesa.2021.106320.

[90] Marrot L, Lefeuvre A, Pontoire B, Bourmaud A, Baley C. Analysis of the hemp fiber mechanical properties and their scattering. Ind Crops Prod 2013;51:317–27. http://dx.doi.org/10.1016/j.indcrop.2013.09.026.

[91] Bourmaud Alain, Morvan Claudine, Bouali Anis, Placet Vincent, Perré Patrick, Baley Christophe. Relationships between micro-fibrillar angle, mechanical properties and biochemical composition of flax fibers. Ind Crops Prod 2013;44:343–51. http://dx.doi.org/10.1016/j.indcrop.2012.11.031.

[92] Li Yan, Ma Hao, Shen Yiou, Li Qian, Zheng Zhuoyuan. Effects of resin inside fiber lumen on the mechanical properties of sisal fiber reinforced composites. Compos Sci Technol 2015;108:32–40. http://dx.doi.org/10.1016/j.compscitech.2015.01.003.

[93] Pantaloni Delphin, Rudolph Anton Loïc, Shah Darshil U, Baley Christophe, Bourmaud Alain. Interfacial and mechanical characterisation of biodegradable polymer-flax fibre composites. Compos Sci Technol 2021;201. http://dx.doi.org/10.1016/j.compscitech.2020.108529.

[94] Oksman Kristiina. High quality flax fibre composites manufactured by the resin transfer moulding process. J Reinf Plast Compos 2001;20:621–7. http://dx.doi.org/10.1177/073168401772678634.

[95] Oksman Kristiina, Wallström Lennart, Berglund Lars A, Filho Romildo Dias Toledo. Morphology and mechanical properties of unidirectional sisal-epoxy composites. J Appl Polym Sci 2002;84:2358–65. http://dx.doi.org/10.1002/app.10475.

[96] Brahim Sami Ben, Cheikh Ridha Ben. Influence of fibre orientation and volume fraction on the tensile properties of unidirectional alfa-polyester composite. Compos Sci Technol 2007;67:140–7. http://dx.doi.org/10.1016/j.compscitech.2005.10.006.

[97] Graupner Nina, Müssig Jörg. A comparison of the mechanical characteristics of kenaf and lyocell fibre reinforced poly(lactic acid) (PLA) and poly(3-hydroxybutyrate) (PHB) composites. Composites A 2011;42:2010–9. http://dx.doi.org/10.1016/j.compositesa.2011.09.007.

[98] Ochi Shinji. Mechanical properties of kenaf fibers and kenaf/PLA composites. Mech Mater 2008;40:446–52. http://dx.doi.org/10.1016/j.mechmat.2007.10.006.

[99] Andersons J, Spārniņš E, Joffe R. Stiffness and strength of flax fiber/polymer matrix composites. Polym Compos 2006;27:221–9. http://dx.doi.org/10.1002/pc.20184.

[100] Bodros Edwin, Pillin Isabelle, Montrelay Nicolas, Baley Christophe. Could biopolymers reinforced by randomly scattered flax fibre be used in structural applications? Compos Sci Technol 2007;67:462–70. http://dx.doi.org/10.1016/j.compscitech.2006.08.024.

[101] Hornsby PR, Hinrichsen E, Tarverdi K. Preparation and properties of polypropylene composites reinforced with wheat and flax straw fibres: Part II analysis of composite microstructure and mechanical properties. J Mater Sci 1997;32:1009–15. http://dx.doi.org/10.1023/A:1018578322498.

[102] Aliotta Laura, Gigante Vito, Coltelli Maria Beatrice, Cinelli Patrizia, Lazzeri Andrea, Seggiani Maurizia. Thermo-mechanical properties of PLA/short flax fiber biocomposites. Appl Sci (Switzerland) 2019;9. http://dx.doi.org/10.3390/app9183797.

[103] Oksman K, Skrifvars M, Selin JF. Natural fibres as reinforcement in polylactic acid (PLA) composites. Compos Sci Technol 2003;63:1317–24. http://dx.doi.org/10.1016/S0266-3538(03)00103-9.

[104] Rana AK, Mandal A, Mitra BC, Jacobson R, Rowell R, Banerjee AN. Short jute fiber-reinforced polypropylene composites: Effect of compatibilizer. J Appl Polym Sci 1998;69:329–38. http://dx.doi.org/10.1002/(SICI)1097-4628(19980711)69:2<329::AID-APP14>3.0.CO;2-R.

[105] Joseph PV, Joseph Kuruvilla, Thomas Sabu. Effect of processing variables on the mechanical properties of sisal-fiber-reinforced polypropylene composites. Compos Sci Technol 1999;59:1625–40. http://dx.doi.org/10.1016/S0266-3538(99)00024-X.

[106] Devi L Uma, Bhagawan SS, Thomas Sabu. Mechanical properties of pineapple leaf fiber-reinforced polyester composites. J Appl Polym Sci 1997;64:1739–48. http://dx.doi.org/10.1002/(SICI)1097-4628(19970531)64:9<1739::AID-APP10>3.0.CO;2-T.

[107] Lu Na, Oza Shubhashini. A comparative study of the mechanical properties of hemp fiber with virgin and recycled high density polyethylene matrix. Composites B 2013;45:1651–6. http://dx.doi.org/10.1016/j.compositesb.2012.09.076.

[108] Laranjeira E, Carvalho LH De, Silva S MDL, D'Almeida J RM. Influence of fiber orientation on the mechanical properties of polyester/jute composites. J Reinf Plast Compos 2006;25:1269–78. http://dx.doi.org/10.1177/0731684406060577.

[109] Thomason JL, Vlug MA, Schipper G, Krikor H GLT. Influence of fibre length and concentration on the properties of glass fibre-reinforced polypropylene: Part 3. Strength and strain at failure. Composites A 1996;27:1075–84. http://dx.doi.org/10.1016/1359-835X(96)00066-8.

[110] Harper LT, Turner TA, Warrior NA, Rudd CD. Characterisation of random carbon fibre composites from a directed fibre preforming process: The effect of fibre length. Composites A 2006;37:1863–78. http://dx.doi.org/10.1016/j.compositesa.2005.12.028.

[111] Jiang Bing, Liu Charlie, Zhang Chuck, Wang Ben, Wang Zhi. The effect of non-symmetric distribution of fiber orientation and aspect ratio on elastic properties of composites. Composites B 2007;38:24–34. http://dx.doi.org/10.1016/j.compositesb.2006.05.002.

[112] Mardia Kanti V, Jupp Peter E. Directional statistics. Wiley; 2009, p. 429.

[113] Lebedev VI. Quadratures on a sphere. USSR Comput Math Math Phys 1976;16:10–24. http://dx.doi.org/10.1016/0041-5553(76)90100-2.

[114] Schjødt-Thomsen J, Pyrz R. The Mori–Tanaka stiffness tensor: Diagonal symmetry, complex fibre orientations and non-dilute volume fractions. Mech Mater 2001;33:531–44. http://dx.doi.org/10.1016/S0167-6636(01)00072-2.

[115] Sevostianov Igor, Kachanov Mark. On some controversial issues in effective field approaches to the problem of the overall elastic properties. Mech Mater 2014;69:93–105. http://dx.doi.org/10.1016/j.mechmat.2013.09.010.

[116] Mura T. Micromechanics of defects in solids, vol. 3, Springer; 1987.

[117] Sevostianov Igor, Yilmaz Nadir, Kushch Vladimir, Levin Valery. Effective elastic properties of matrix composites with transversely-isotropic phases. Int J Solids Struct 2005;42:455–76. http://dx.doi.org/10.1016/j.ijsolstr.2004.06.047.

[118] Lee Sangryun, Ryu Seunghwa. Theoretical study of the effective modulus of a composite considering the orientation distribution of the fillers and the interfacial damage. Eur J Mech A Solids 2018;72:79–87. http://dx.doi.org/10.1016/j.euromechsol.2018.02.008.